Available online at www.sciencedirect.com

ScienceDirect

Green Energy & Environment 2 (2017) 218–245

www.keaipublishing.com/gee

Review article

Synthesis and applications of MOF-derived porous nanostructures

Min Hui Yap [a], Kam Loon Fow [a,*], George Zheng Chen [a,b,*]

[a] Department of Chemical and Environmental Engineering, and Energy Engineering Research Group, Faculty of Science and Engineering, University of Nottingham Ningbo China, 199 Taikang East Road, Ningbo 315100, China

[b] Department of Chemical and Environmental Engineering, and Advanced Materials Research Group, Faculty of Engineering, University of Nottingham, Nottingham NG7 2RD, UK

Received 31 March 2017; revised 17 May 2017; accepted 17 May 2017
Available online 25 May 2017

Abstract

Metal organic frameworks (MOFs) represent a class of porous material which is formed by strong bonds between metal ions and organic linkers. By careful selection of constituents, MOFs can exhibit very high surface area, large pore volume, and excellent chemical stability. Research on synthesis, structures and properties of various MOFs has shown that they are promising materials for many applications, such as energy storage, gas storage, heterogeneous catalysis and sensing. Apart from direct use, MOFs have also been used as support substrates for nanomaterials or as sacrificial templates/precursors for preparation of various functional nanostructures. In this review, we aim to present the most recent development of MOFs as precursors for the preparation of various nanostructures and their potential applications in energy-related devices and processes. Specifically, this present survey intends to push the boundaries and covers the literatures from the year 2013 to early 2017, on supercapacitors, lithium ion batteries, electrocatalysts, photocatalyst, gas sensing, water treatment, solar cells, and carbon dioxide capture. Finally, an outlook in terms of future challenges and potential prospects towards industrial applications are also discussed.

Keywords: Metal organic frameworks; Porous nanostructures; Supercapacitors; Lithium ion batteries; Heterogeneous catalyst

1. Introduction

1.1. Metal organic frameworks (MOFs)

Porous materials such as porous ceramics, zeolites, activated charcoals, porous metal, polymer foams, and porous glass are being used in many ways in our daily lives. Due to their well-known properties and wide range applications, the field of porous materials, in particular the nanoporous materials, has undergone rapid development in the past two decades. Among the recent developed porous materials, metal organic frameworks (MOFs) are distinct from other traditional porous materials because of their high porosity and thermal stability. Formed by the three-dimensional crystalline assembly of inorganic metal ions and organic ligands, MOFs enable flexible structure design of which well-defined pore sizes, surfaces areas and functionalities can be tailored by selecting different building blocks. This high degree of customizability of MOFs properties has attracted the interest of many researchers. To date, there are more than 20,000 different structures of MOFs being reported and studied [1]. A few examples of different MOFs structures are illustrated in Fig. 1.

Depending on the final structures and properties, MOFs may be prepared using several distinct synthetic methods such as: slow diffusion [3], hydrothermal (solvothermal) [4], electrochemical [5], mechanochemical [6], microwave assisted heating and ultrasound [7]. These synthesis methods and formation

* Corresponding authors. Department of Chemical and Environmental Engineering, and Advanced Materials Research Group, Faculty of Engineering, University of Nottingham, Nottingham NG7 2RD, UK.

E-mail addresses: Kam-Loon.Fow@nottingham.edu.cn (K.L. Fow), george.chen@nottingham.ac.uk (G.Z. Chen).

http://dx.doi.org/10.1016/j.gee.2017.05.003

List of abbreviations

MOFs	Metal organic frameworks
ZIF	Zeolitic imidazolate framework
EDLCs	Electric double-layer capacitors
LIBs	Lithium ion batteries
MWCNTs	Multi-walled carbon nanotubes
TEM	Transmission electron microscopy
NPC	Nitrogen-doped porous carbon
NPM	Non-precious metal
AQ	Anthraquinone
NQ	1,4-napthoquinone
TCBQ	Tetrachlorobenzoquinone
BDC	1,4-benzenedicarboxylic acid
BTC	1,3,5-benzenetricarboxylic acid
NTCDA	1,4,5,8-naphthalenetetracarboxylic dianhydride
PTCDA	Perylene-3,4,9,10-tetracarboxylic dianhydride
MMT	Montmorillonite
RHE	Reversible hydrogen electrode
SCE	Saturated calomel electrode

mechanisms of MOFs have been comprehensively reviewed by Seoane and co-workers recently [8]. A wide range of potential applications of MOFs, ranging from gas (e.g. hydrogen) storage and separation, sensing, catalysis, to drug delivery, has also been reviewed [9,10]. After nearly three decades since the first report on synthesis MOFs [11], a few MOFs are now produced commercially. One of the most prominent commercialized MOFs is Cu-BTC (also known as HKUST-1) produced by BASF (marketed under the trademark BASOLITE® C 300) and sold by Sigma Aldrich [2]. Among other companies which hold patents for large scale synthesis of MOFs are MOF Technologies, Ford Global Technologies, Toyota, and Strem Chemicals. A search on the World Intellectual Property Organization (WIPO) database revealed a constant increment of the number of patents published by the world-wide research community. This indicates that MOFs are gaining a considerable momentum towards commercial applications. The number of patent publications from the years 2007–2017 and the number of patents filed by each country are shown in Figs. 2 and 3, respectively. These patents cover the production and applications of various MOFs or their composites. Fig. 3 also highlights that the top two highest numbers of patents are filed by innovators from United States and China. This is a clear evidence that the researchers from these two countries are committed to the exploration of the commercial opportunities of MOFs. On the other hand, according to the WIPO database, the company which currently owns the highest number of patents is BASF, with 133 patents published so far.

In addition, the huge library of MOFs structures and the optimized synthesis methods are helpful for researchers to explore some other potential applications of MOFs, such as the usage of MOFs as sacrificial materials for the synthesis of various nanostructures. This has opened a new direction in application of MOFs, and might contribute to a better understanding of the properties of porous materials. It is evident that many of the papers published from the years 2008–2013 are short communications or research work focusing on the synthesis of various new nanostructures from MOFs and determination of the basic physical properties of the resultant structures. Very few have measured the performance of these materials against specific applications and study their recyclability. The synthesis method of nanostructures from MOFs has been reviewed thoroughly by Mai et al. [12]. However, to the best of our knowledge, there is not yet a review that is specifically devoted to the synthesis and characterizations of MOFs-derived nanostructures for applications in energy related materials, devices, and processes. For this very reason, we intend to seize this opportunity to review on recent advances in MOF-derived nanostructures for energy-related applications from the years 2013–2017, and to anticipate the prospects of these MOF-derived nanostructures.

1.2. Synthesis of various nanostructures from MOFs

Porous carbon, metals, metal oxides, and their multicomponent hybrids are important inorganic materials for energy and environmental applications. Dependent on the desired application purposes, porous materials can be prepared by several synthetic approaches such as hard templating and soft templating. Hard templating method involves the framework precursors filling the cavities present in the structured solid template of which the template can be removed from the porous structure after synthesis. In comparison, soft templating method involves a more subtle physical or chemical interactions between framework source and template which direct the self-assembly synthesis to allow better control of the material properties [13]. When compared between these two templating approaches, soft templating provides a more successful pathway for the synthesis of ordered and disordered porous matrices [14]. In the soft templating route, porous materials are generally synthesized using the solvothermal method. This solvothermal method is also the most preferred method for large scale production, owing to its relative simplicity and scalability. Aside being used for the synthesis of zeolite, the concept of solvothermal synthesis method has also been applied with great success for the synthesis of MOFs.

In the context of synthesizing various nanostructures from MOFs, MOFs can act as a precursor in which the metal components provide an intrinsic metal source to derive nanostructures of metals or metals oxides, as well as a self-sacrificing template, in which the organic components can be used as a carbon source to prepare nanoporous carbon [15]. In general, certain MOF structures, such as Cu-BTC and MOF-5, are collapsed during the carbonization process, whereas other MOF structures, such as ZIF-8 and ZIF-67, are better in providing a template to guide the formation of pores by allowing evaporation of confined organic moistures during pyrolysis, resulting in a spongy-pore system. Nevertheless, a homogeneous distribution of nanoparticles in their respective

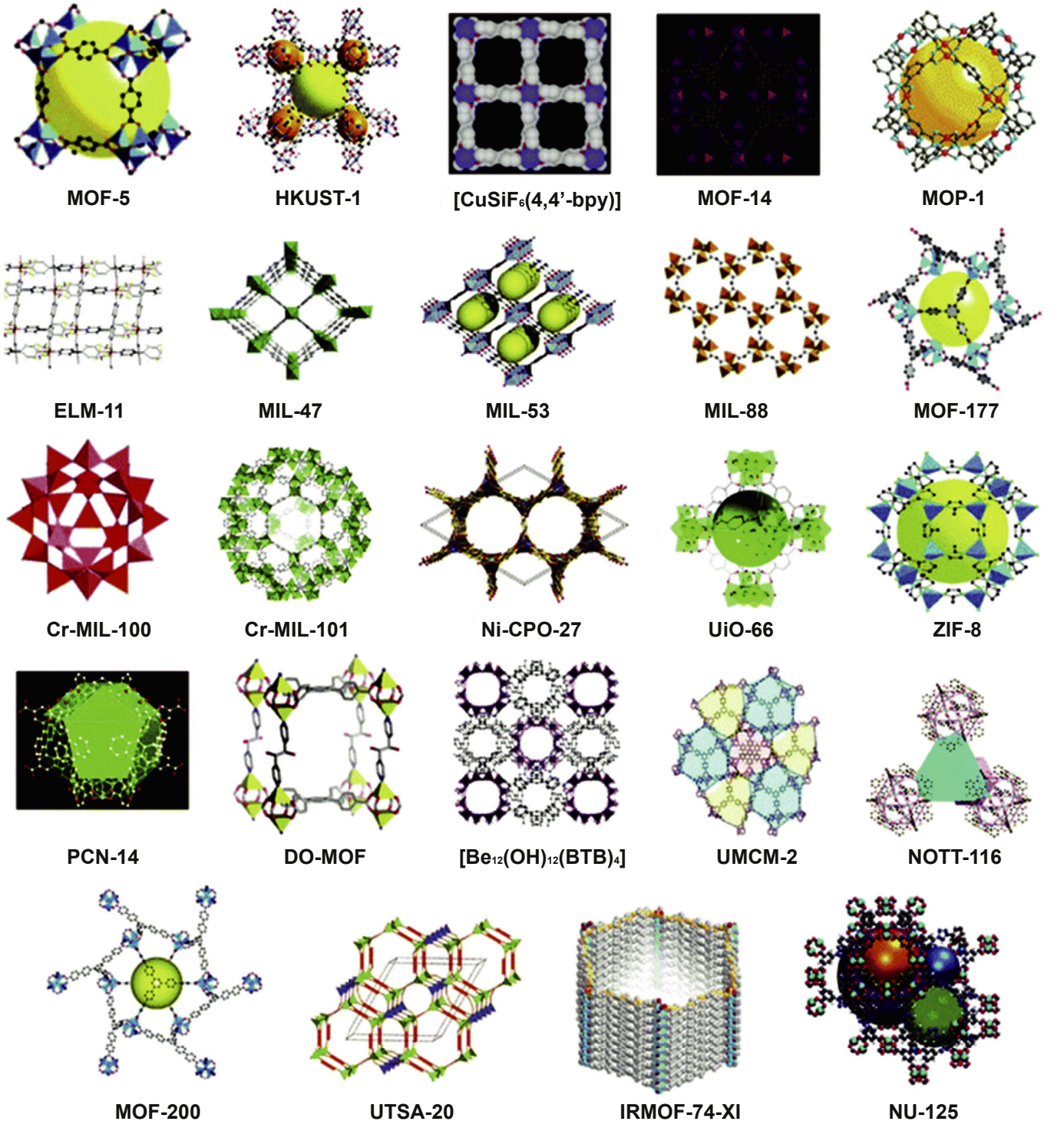

Fig. 1. Illustration of nanoporous structures of different MOFs synthesized by different research groups. Reproduced from Ref. [2], with permission from the Royal Society of Chemistry.

medium is expected. Some of the advantages of using MOFs as a precursor/sacrificial template for preparation of various nanostructures include, but not limited to,

i) the fabrication of MOF-derived nanostructures with desired topological textures and material properties are made possible with the controlled-calcination of MOFs
ii) undesired structural collapse of the framework during calcination can be reduced with the use of MOFs as templates since they generally show structural robustness [16]
iii) allow easy functionalization with other heteroatoms and metal/metal oxides, therefore able to increase overall performance and efficiency
iv) the preparation of MOFs can be carried out under mild conditions and simple processes

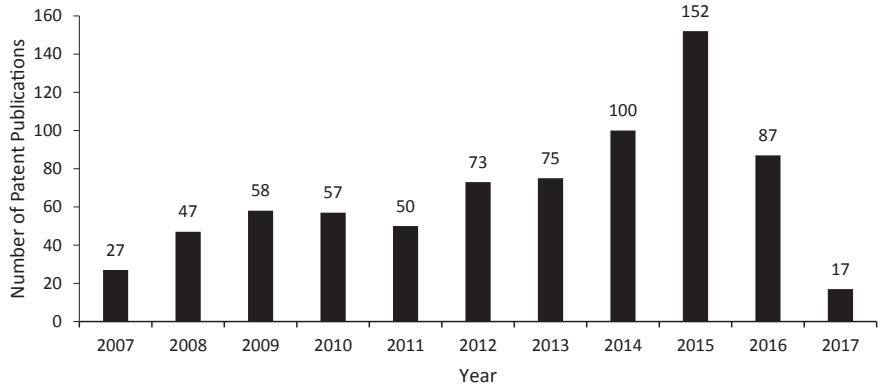

Fig. 2. Number of patent publications from 2007 to 2017, according to the World Intellectual Property Organization database. (Search Terms: metal organic framework).

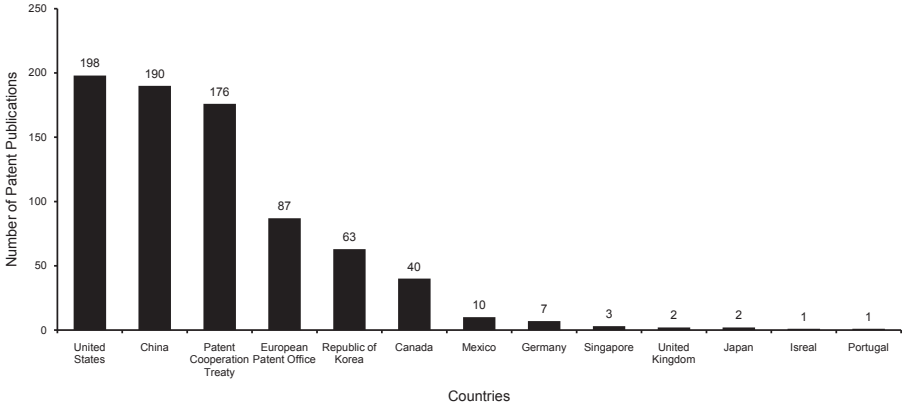

Fig. 3. Number of patent publications by countries according to the World Intellectual Property Organization database, from 2007 to 2017. (Search Terms: metal organic framework).

Benefiting from these advantages, MOF-derived nanostructures have narrower distributions of pore volumes, and higher specific surface area, and have more variations in morphology, such as nanocages, hollow spheres, and hollow polyhedrons, compared to other nanostructures. Additionally, this synthesis approach also helps solve the potential incompatibility issue between electroactive material and 3D substrate support through some unique growth and decomposition mechanisms. However, on-going research is aiming to address and overcome the limitations of using MOF as precursors/templates. Some of these limitations include poor control of the pore size of the MOF-derived nanostructures due to the lack of understanding of the MOF decomposition mechanisms, and relatively high calcination temperatures are required.

Notably, by subjecting MOF precursors of various structures and crystallinity to different calcination temperatures, material with different topologies, crystallographic phases, and porosities can be obtained. Fig. 4 shows the overview of different types of nanostructures synthesized from thermal treatment of MOF precursors. It is worth mentioned that ion-exchange method has also emerged recently as an alternative method to thermal treatment for preparation of various nanostructures from MOF precursors. Although more chemicals and experimental steps were involved in the ion-exchange method, nevertheless, the as-synthesized nanostructures from this method have demonstrated some exciting properties [30,32,58].

Overall, this article aims to present a comprehensive review on the recent development in the synthesis and applications of various nanostructures derived from different MOFs. In the subsequent sections, we will summarize some recent exciting examples of these applications across the field of electrochemical energy storage, catalysis, sensing, and water treatment.

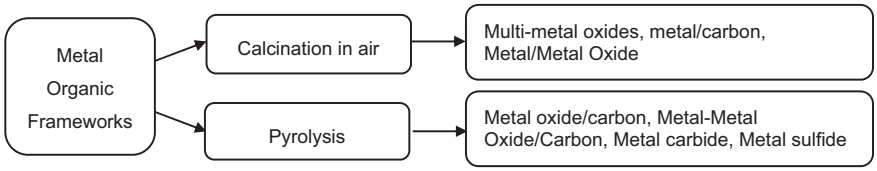

Fig. 4. Overview of different types of nanostructures derived from MOFs Precursor.

2. Applications of MOF-derived nanostructures in electrochemical energy storage

The demand for efficient use of clean and renewable energy, as well as, the popularization of portable electronics and electric vehicles has prompted the development of energy storage materials, especially for electrochemical energy storage [17]. The use of nanomaterials for electrochemical energy storage has emerged as a promising approach [18]. Given their unique electrical, mechanical properties, and high surface area, nano-sized active materials are expected to bridge the gap towards the realization of the next generation of energy storage device [19]. For being competitive, these materials also need to have long cycle-life, good charge/discharge efficiency, good retention of charge and adequate operate voltage to ensure high energy and power density of the storage devices [20]. Many investigations had been carried out in the search for a better synthesis method for producing materials to cater different electrochemical energy storage purposes. The direct pyrolysis/carbonization of MOFs is a new method for synthesis of porous materials for energy storage. The use of pristine MOF and MOF-derived structures for electrochemical energy storage and conversion has been reviewed by Xia and co-workers in early 2015 [17]. Nonetheless, this review will cover the MOF-derived nanostructures and their applications as electrode materials for supercapacitors and LIBs, with a focus of more recent works published between 2015 and 2017. In order to compare and show the classifications of various electrochemical energy storage devices, a graphical illustration of a simplified Ragone plot of specific power versus specific energy is shown in Fig. 5.

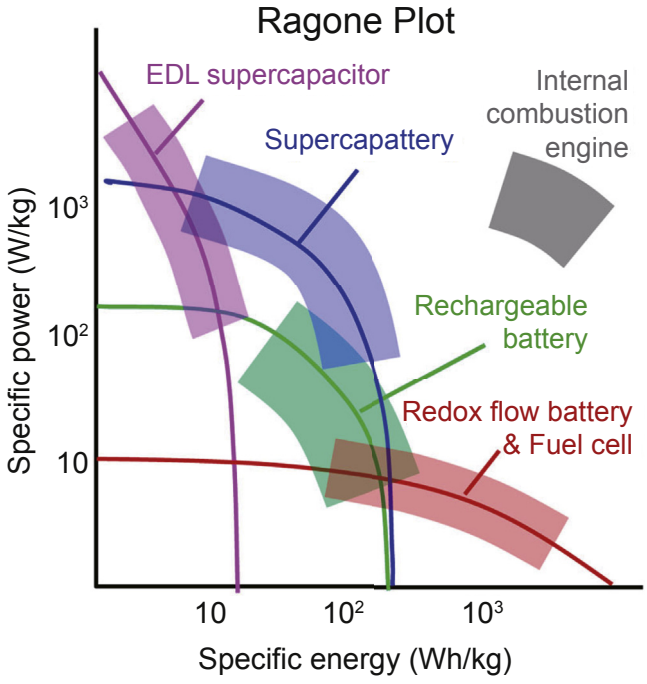

Fig. 5. Illustrative Ragone plots of specific power versus specific energy for the various electrochemical energy storage devices and internal combustion engine [21].

2.1. Supercapacitors

A capacitor is a passive component designed to store energy in an electric field. It generally consists of two conducting plates separated by an insulator (dielectric) [21,22]. A supercapacitor (electrochemical capacitor), on the other hand, is an ideal electrical energy storage device with higher power capability, longer cyclic life, and higher packaging flexibility compared to traditional energy storage devices [23]. Presently, there are two types of supercapacitors, namely: the electric double-layer capacitors (EDLCs) and pseudocapacitors (which employ a reversible Faradaic reaction to store charges) [21,24]. Carbon materials are commonly used as electrode materials for EDLCs. However, they do not have very high specific capacitance despite their high surface area. The incorporation of heteroatoms such as nitrogen or oxygen into the carbon structures can improve the capacitive storage of the carbonaceous materials. This is well demonstrated by Zhong and co-workers, who prepared a series of nitrogen-doped porous carbon (NPC) from ZIF-8 (prepared from zinc salts and 2-methylimidazole) with the addition of carbon sources (melamine, urea, xylitol and sucrose) [25]. Their results proved that the introduction of additional carbon sources would form a protective layer around the samples, thus reducing their nitrogen loss during carbonization. This was evident from the fact that the NPC sample with the highest nitrogen content (4.5 wt.%) had the best capacitive behavior (285.8 F g^{-1} at a mass normalized current of 0.1 A g^{-1}).

Aside from nitrogen doping and carbon capping, another strategy that could increase the performance of MOF-based carbon materials is support modification and redox-active molecules functionalization. In the year 2016, Wang's team coated ZIF-8 derived carbon onto multi-walled carbon nanotubes (MWCNTs) to form necklace-like structures [26]. The schematic illustration for the synthesis of C@MWCNTs, its resultant TEM image, and the specific capacitances at different current densities are illustrated in Fig. 6. The synthesis began by stirring a mixture solution of ZIF-8 and MWCNTs, kept still for 24 h, then followed by annealing at 800 °C for 3 h. After carbonization, the porous carbons were embedded on the surface of crystalline MWCNTs, as evident from the TEM image (Fig. 6). When compared to other core–shell structures and MWCNTs based core–shell structures, this MOF-derived C@MWCNTs provide some extra accessible surfaces for ion transports which does not agglomerate or restack. The MOF-derived nanostructures have some improved performances, such as high specific capacitance (326 F g^{-1} at a mass normalized current of 1 A g^{-1}), good rate capability, and excellent cycling stability (99.7% capacitance retention after 10,000 cycles).

Guo's group had attempted the functionalization of some NPC materials by the incorporation of anthraquinone (AQ), 1,4-napthoquinone (NQ), and tetrachlorobenzoquinone (TCBQ) to the NPC framework via a noncovalent interactions method [27]. Results indicated that AQ-NPC had the best current response in the negative potential region with a specific capacitance of 373 F g^{-1} at a mass normalized current of 1 A g^{-1}, whereas a variant combination, (TCBQ + NQ)-NPC,

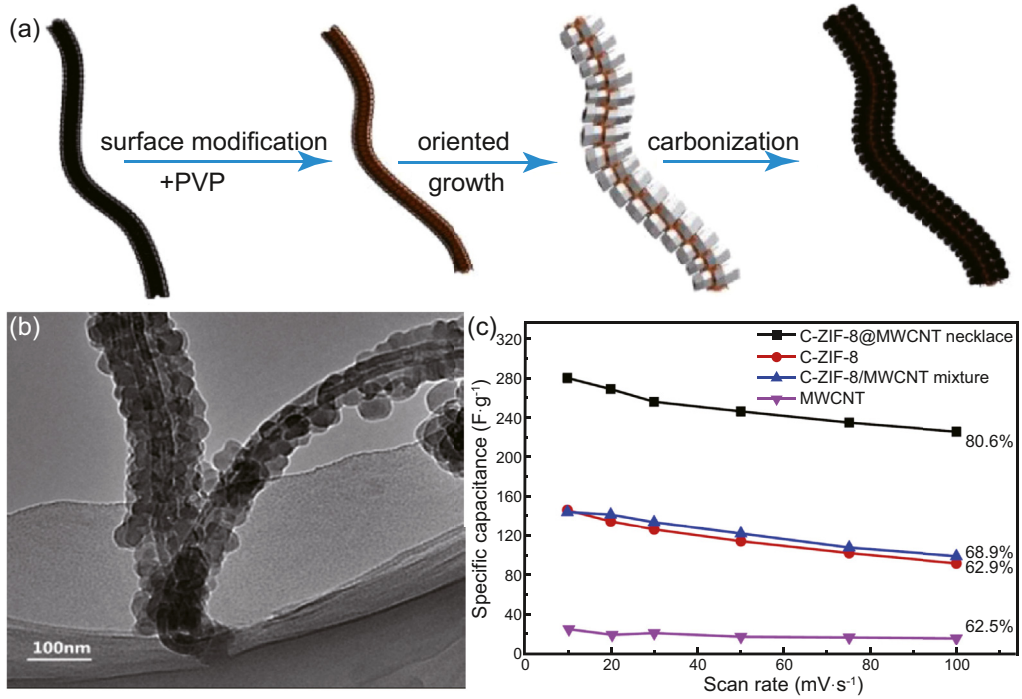

Fig. 6. Schematic illustration for (a) the synthesis of C@MWCNTs, (b) its resultant TEM image, and (c) the specific capacitances at different current densities. Reproduced from Ref. [26], with permission from Elsevier.

showed a current response in the positive potential region. Together they generated a potential self-matching behavior in the two-electrode configuration, which led to a high performance asymmetrical supercapacitor with a high specific energy value of 23.5 Wh kg^{-1}. More importantly, this functionalized method had enhanced the overall capacitance of carbon by 1.4 times.

In general, the performance of carbon-based materials as EDLC is affected by pore size distribution and pore volume. On the other hand, the redox active species for Faradaic capacitors are dependent on the size of the redox active species, porosity, crystallinity and surface area of the electrode materials for energy storage [17]. Redox active species are transition metal oxides or conductive polymers which have a storage mechanism based on reversible Faradaic redox reactions. The preparation of redox active species using MOF precursors are less common compared to the preparation of carbon materials from MOFs.

In 2014, Zhang's team described the calcination of ZIF-67 (prepared from cobalt salts and 2-methylimidazole) in air at 450 °C for 30 min (with a slow heating rate of 1 °C/min) for the preparation of porous hollow Co_3O_4 with rhombic dodecahedral structures [28]. This hollow rhombic structure provided structural stability for the charging/discharging cycle whereas the highly mesoporous Co_3O_4 structures enabled the facile penetration of electrolyte and guaranteed a relatively high electroactive surface area. These properties had successfully increased the overall rate capacity and cycle life of the hollow Co_3O_4 nanoparticles. These nanoparticles reported a remarkable specific capacitance of 1100 F g^{-1} at a high mass normalized current of 12.5 A g^{-1}.

The incorporation of Ni^{2+} cations, S^{2-} anions or OH^- anions could increase electrical conductivity and aid the formation of new active sites. In 2015, Hu's group synthesized $Co_3O_4/NiCo_2O_4$ double shelled nanocages from ZIF-67 and Ni–Co layered double hydroxides (source of Ni^{2+} cations) [29]. The formation process of these nanocages is shown in Fig. 7. The as-synthesized materials were evaluated as electrodes for pseudo capacitors and electrocatalysts for oxygen generation. Results showed that the $Co_3O_4/NiCo_2O_4$ nanocages exhibited a high capacitance of 972 F g^{-1} at 5 A g^{-1} and even an impressive 615 F g^{-1} of capacitance at 50 A g^{-1}. A superior cycling stability of 12,000 cycle life was also achieved. Besides that, as an electrocatalyst, the bimetallic nanocages delivered a current density of 10 mA cm^{-2} at a potential of 1.57 V vs. reversible hydrogen electrode (RHE). The greatly enhanced performance was attributed to the composition and complex structure of the double shelled nanocages and the incorporation of Ni^{2+} cations. On the other hand, the incorporation of S^{2-} anions to the nanostructures was demonstrated by Jiang's team who fabricated hollow CoS nanocages from ZIF-67 template and thioacetamide using ion-exchange method [30]. Even though the cycling stability was not high, however, these CoS polyhedral nanocages had the highest reported specific capacitance among those nanostructures discussed in this Section 2.1 (~1400 F g^{-1} at a mass normalized current of 10 A g^{-1}). The study had successfully proved the importance of S^{2-} hydrolyzing of ZIF-67 and the effectiveness of using MOF template in producing nanostructures with high performing pseudo capacitance properties. Hu and co-workers worked on a similar method of using ZIF-67 to produce CoS nanocages but added an additional step of reaction with water

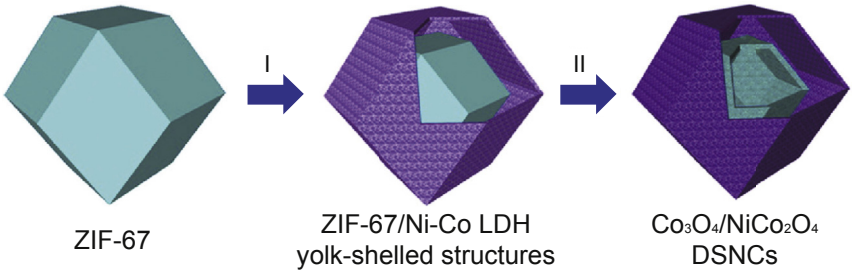

Fig. 7. Schematic illustration of the formation process of $Co_3O_4/NiCo_2O_4$ double shelled nanocages. Reproduced from Ref. [29], with permission from American Chemical Society.

(OH^- anions) to obtain double-shelled hollow CoS nanostructures surrounded by outer CoS nanosheet-constructed shells [31]. Without the presence of carbon, the double-shelled hollow structures had showed a large specific surface area of 11 $m^2\ g^{-1}$. Not only did the double-shelled assembly supply more active sites for electrochemical reactions, it also resulted in good structural robustness to enhance electrochemical stability. The stability of CoS was demonstrated when a specific capacitance of 765.6 F g^{-1} (at a mass normalized current of 10 A g^{-1}) was achieved after 10,000 cycles. Recently, Guan's team carried out two ion-exchange reactions (with S^{2-} anions and then with Ni^{2+} cations) to obtain onion-like $NiCo_2S_4$ particle from a Co-MOF [32]. Remarkably, the seven-layered onion-like structure delivered better rate performance, higher energy density, higher power density, and comparable capacitance retention (after tested for 10,000 cycles) than those Ni–Co sulfide based electrodes derived from non-MOF template reported in Ref [33–35]. Benefiting from the complex composition and multi-shelled structure, a specific capacitance of 765.6 F g^{-1} was achieved after 10,000 cycles at a mass normalized current of 10 A g^{-1}.

Furthermore, among the novel MOF-derived redox active species, the binary mixed metal/metal oxide@carbon composites prepared by Wang and co-workers had showed excellent super capacitive performance [36]. The group carbonized Co–Mn-MOF-74 nanoparticles at 600–800 °C under nitrogen flow for 2 h to obtained Co–CoO–MnO@C composites. The schematic illustration for the preparation of Co–CoO–MnO@C composites is shown in Fig. 8. At a pyrolysis temperature of 700 °C, the porous electrode delivered a maximum specific capacitance of 800 F g^{-1} at a mass normalized current of 1 A g^{-1}. The reasons for such good result included the support gained from embedment of metal oxides particles in the carbon framework, more active contact area provided from the uniform dispersion of active metal oxide nanoparticles, and reduced transport length, faster electrons transport, and better charge–discharge efficiency provided by porous carbon framework (from the original MOF framework).

Given the effectiveness and relatively straightforward synthesis procedures, other researchers had also employed this method for the synthesis of various other metal/metal oxides. In 2017, Han's team fabricated NiO (from Ni-MOF) with a reversible specific capacitance of 324 F g^{-1} at a mass normalized current of 1 A g^{-1} [37]. Comparatively, Wu and Hsu embedded Ni nanoparticles in partially graphitic porous carbon and found that it had much superior capacitive behavior [38]. Optimization was carried out to increase electrical conductivity while maintaining large surface area. At the end, NiO nanoparticles synthesized from an optimum pyrolysis temperature of 800 °C, was able to achieve a reversible specific capacitance of 886 F g^{-1} at a mass normalized current of 1 A g^{-1}. These well-dispersed NiO nanoparticles also provided extra redox capacitance for Faradaic reactions.

Meanwhile, Zeng and co-workers reported the room temperature synthesis of CeO_2 from Ce-BTC (prepared from cerium salts and benzene-1,3,5-tricarboxylic acid (BTC)) by treatment of Ce-BTC in an alkaline solution of KOH for 2 h [39]. SEM images of both structures are shown in Fig. 9. After alkali treatment, some of the original dumbbell-shaped from Ce-BTC remained, while some collapsed into half dumbbell-shaped

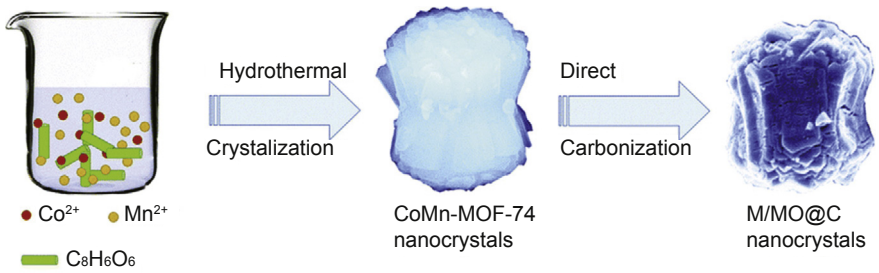

Fig. 8. Schematic illustration for the preparation of Co–CoO–MnO@C composites and SEM image of Co–CoO–MnO@C composites. Reproduced from Ref. [36], with permission from The Royal Society of Chemistry.

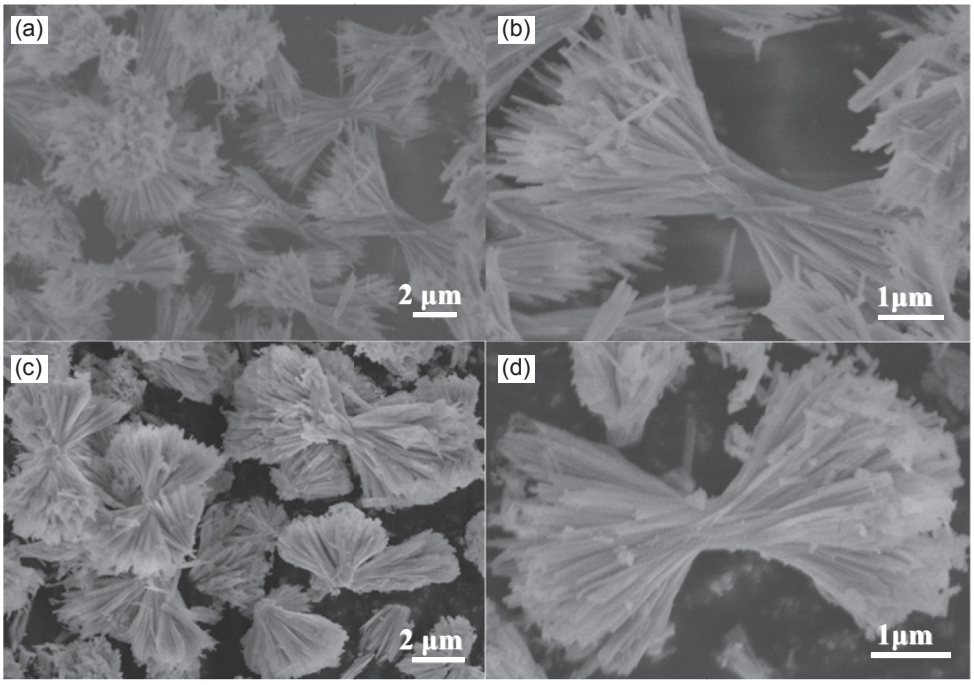

Fig. 9. SEM images of (a–b) Ce-MOF and (c–d) CeO_2. Reproduced from Ref. [39], with permission from Elsevier.

structures. Nevertheless, CeO_2 had demonstrated a remarkable stability up to 10,000 cycles and a capacitive performance of 235 F g^{-1}. This specific capacitance of this CeO_2 can also be increased more than three-fold to 779 F g^{-1} with the addition of $K_4Fe(CN)_6$ (redox-active agent) into the alkali KOH solution. Lastly, the electrochemical capacitive performance MOF-derived Cr_2O_3 – carbon composite was also studied by Ullah's group [40]. The as-synthesized nanocomposites exhibited a specific capacitance of 291 F g^{-1} at a mass normalized current of 0.25 A g^{-1} and a 95.5% long-term cycling stability over 3000 cycles. The porosity and high surface area of the composites obtained using this approach had made them promising electrode material for use as supercapacitors.

In summary, despite their disadvantages such as lower specific capacitance and lower power density, MOF-derived carbon, metal oxides, and their composites have promising applications in supercapacitors. In general, ZIF-8 derived carbon has the largest surface area, whereas Co-MOF derived nanostructures exhibit the highest specific capacitance. A more detailed comparison of the performance of various nanostructures synthesized from MOF precursors as supercapacitors, which are discussed in this section, is summarized in Table 1 and graphically presented in Fig. 10. The strategies which are crucial for improvement of supercapacitive performance could be summarized as: i) well dispersion of nanoparticles, ii) presence of porous carbon framework (or hollow

Table 1
Comparison of the performance of various nanostructures synthesized from MOF precursors as supercapacitors.

Materials	Doping	Original MOF	Specific surface area (m^2 g^{-1})	Mass normalized current (A g^{-1})	Specific capacitance (F g^{-1})	Cycle numbers	Reference
Carbon	Nitrogen	ZIF-8	934	0.1	285.8	1000	[25]
Functionalized C	Nitrogen	ZIF-8	1140	1	373	5000	[27]
C@MWCNT	–	ZIF-8	569.3	1.0	326.0	10,000	[26]
Co_3O_4	–	ZIF-67	128	12.5	1100	6000	[28]
$Co_3O_4/NiCo_2O_4$	Nickel	ZIF-67	46	5	972	12,000	[29]
CoS	Sulfur	ZIF-67	96.3	10	~1400	1000	[30]
Double-shelled CoS	Hydroxide, Sulfur	ZIF-67	110	5	769.9	10,000	[31]
$NiCo_2S_4$	Sulfur, Nickel	Co-MOF	72	10	765.6	10,000	[32]
Co/MnO/CoO/C	–	CoMn-MOF-74	242.4	1	800	1000	[36]
NiO	–	$Ni_3(HCOO)_6$	34	1	324	1000	[37]
Ni@Graphitic C	–	Ni-BDC	140	1	886	1000	[38]
CeO_2	–	Ce-BTC	205	1	779	10,000	[39]
Cr_2O_3	Carbon	MIL-101	438	0.25	291	3000	[40]

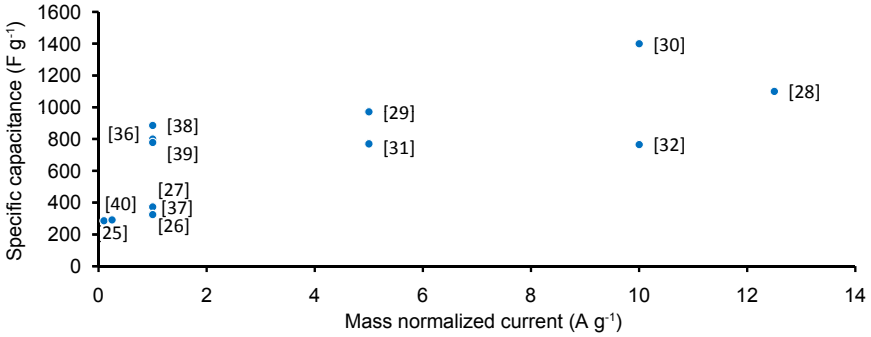

Fig. 10. Comparison of the performance of various nanostructures synthesized from MOF precursors as supercapacitors [denoted by their reference number].

shells) which provide support to hold nanoparticles and larger channels for easy transport of electrolyte ions, iii) addition of nitrogen or other doping to improve electrical conductivity, and iv) presence of a conductive network which facilitate the transport of electrons.

2.2. Lithium ion batteries

Lithium ion batteries (LIBs) are the most vital system for state-of-the art rechargeable batteries. However, despite their long lifespan and ease of integration into portable devices, they are not able to meet the requirements for higher energy and power demand nowadays [41]. In the recent years, aside from graphite, the commercial negative electrode material, various nanostructured materials such as carbon nanotubes, graphene composites, transition metal oxides, etc. have been extensively investigated for applications in LIBs. The quest for these alternative materials is motivated by the limited capacity and energy density of graphite.

Previous works have demonstrated that the incorporation of nitrogen atoms into the carbon networks could facilitate the formation of stronger interaction between the nitrogen-doped carbon structure and the lithium ions [42,43]. In 2014, Zheng and co-workers synthesized NPC from the pyrolysis of ZIF-8 under nitrogen flow [44]. The team manipulated the nitrogen content to improve the electrochemical performance without sacrificing the structural stability of the NPC. At an optimized nitrogen content of 17.72 wt.% and carbonization temperature of 800 °C, the synthesized materials achieved a specific capacity of 2132 mAh g^{-1} after 50 cycles at a mass normalized current of 100 mA g^{-1}. This facile MOF-carbonization method had produced excellent capacity more superior than other NPC materials reported in Ref [45] and [43].

Besides carbon materials, MOFs have also been used as precursors for the fabrication of metal oxides, transition metal oxides, metal/metal oxides, and metal oxides/carbon composites for LIB negative electrode materials. Earlier in 2013, Yang's team examined the synthesis of porous carbon-coated ZnO quantum dots from the controlled pyrolysis of Zn_4O-MOF-5 [46]. The as-synthesized material achieved a high reversible capacity of 1200 mAh g^{-1} at a mass normalized current of 75 mA g^{-1}. As such, this study revealed the importance of optimization of pyrolysis temperature, duration of heating, and the heating rate, because these properties directly affected the crystal size of the ZnO particles, which in turn affected the rate of lithium ions diffusion and the overall electrochemical performance. ZnO quantum dots supported on graphene produced by MOF precursor had also shown better performance compared to those synthesized using atomic layer deposition method, which had a recorded reversible capacity of 960 mAh g^{-1} at a mass normalized current of 100 mA g^{-1}, reported in Ref. [47].

Recently, Song and co-workers synthesized a hollow porous ZnO distributed evenly on carbon nanocages at a moderate pyrolysis temperature of 500 °C [48]. A schematic illustration of their preparation process is shown in Fig. 11. Given its pristine structure which effectively accommodated the agglomeration of ZnO and volume expansion/shrinkage during discharge/charge process, the prepared materials had demonstrated higher specific capacity compared to cobalt-doped ZnO@C reported in Ref. [49]. At a similar mass normalized current of 100 mA g^{-1}, a hollow ZnO@C had a reversible capacity of 750 mAh g^{-1} over 100 cycles, whereas a cobalt-doped ZnO@C had a reversible capacity of 725 mAh g^{-1} over 50 cycles only.

Furthermore, Gao and co-workers have attempted the synthesis of ZnO@C using formic acid as an organic ligand instead of the usual terephthalic acid (H_2BDC) and tested its

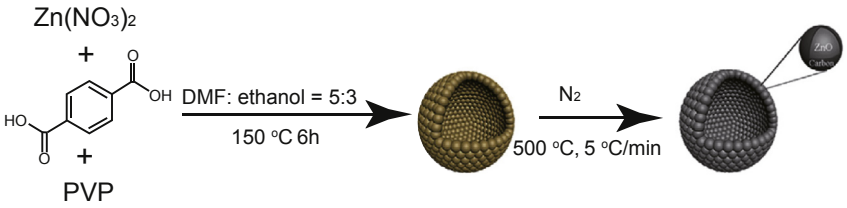

Fig. 11. Schematic illustration of the preparation process of the hollow porous ZnO/C nanocomposites. Reproduced from Ref. [48], with permission from Elsevier.

performance as negative electrode materials for LIB [50]. Results (Entry 5, Table 2) showed that it has better reversible capacity than those prepared from MOFs containing H_2BDC. The authors attributed the excellent stability and lithium ion storage properties to the carbon support and the appropriate carbon content matrix from formic acid which suppressed the agglomeration and growth of ZnO nanoparticles during cycling process. In 2016, Zou's group dispersed porous ZnO nanoparticles (derived from ZIF-8) on MWCNTs [51]. When using methylimidazole as organic ligands and carbon nanotubes as support, the resultant material exhibited a lower reversible capacity of 419.8 mAh g^{-1} at a mass normalized current of 200 mA g^{-1}, but it showed excellent rate capability when tested at various current rate between 100 and 1000 mA g^{-1}. Even when the mass normalized current was increased to 1000 mA g^{-1}, the material was able to retain a specific capacity of 326.8 mAh g^{-1}.

The aforementioned examples demonstrate that ZnO can be synthesized from various Zn-MOFs. By manipulating the choice of organic ligands, pyrolysis conditions, and choice of support, ZnO with different pore sizes and specific capacity can be synthesized. Besides ZnO, ternary Zn-based oxides have also generated much research because of their high specific capacity, low cost, and environmental friendliness. Challenges remained as to improve their inherent poor electrical conductivity and large volume changes upon cycling. In 2014, Zou's group fabricated a novel porous ternary Zn-based oxides, ZnO–$ZnFe_2O_4$@C hybrid structures which had one of the most outstanding electrochemical lithium storage performance reported so far [52]. At optimum conditions, a reversible capacity of 1060 mAh g^{-1} at 500 mA g^{-1} mass normalized current was achieved. This high rate performance was attributed to the near equal molar ratio of Zn to Fe, and the incorporation of nanoparticles in carbon matrix with hollow spaces which helped to relieve the volume effect and maintained the electrical connectivity integrity. Recently, Cai's group synthesized similar ZnO/$ZnFe_2O_4$ hybrid nanostructures but with ZnFe Prussian blue analogue and without a carbon support [53]. This unique structure had displayed a high reversible discharge capacity of 704 mAh g^{-1} after 200 cycles at 200 mA g^{-1}. The synergistic effect from the two well-distributed ZnO and $ZnFe_2O_4$ phases within the hybrid nanostructures have contributed to this superior cycling stability at high mass normalized current. Moreover, this study had proven the potential applications of various MOFs in preparation of hybrid nanostructures with excellent electrochemical performance as negative electrode materials.

In addition to ZnO, Co_3O_4 is another metal oxides which has high theoretical capacities (890 mAh g^{-1}) [54]. In 2017, Du and co-workers employed a controlled calcination of Zn-doped MOF-74 at 400 °C to fabricate porous $ZnCo_2O_4$ [54]. When compared with Co_3O_4, the obtained porous nanostructured $ZnCo_2O_4$ has demonstrated improved specific capacity, cycling stability, and rate capability, owing to the strong synergistic effect between Zn and Co. It was shown that with an additional doping step during MOF synthesis, the pyrolysis of MOF could yield metal/metal oxide compounds with superior properties. Knowing that Co_3O_4 have limited cycling stability and rate capability, Su's team has employed a new strategy to overcome these limitations. They synthesized Co-MOFs with different organic linkers (1,4,5,8-naphthalenetetracarboxylic dianhydride (NTCDA) and perylene-3,4,9,10-tetracarboxylic dianhydride (PTCDA)) and then treated them with organic amine solution before

Table 2
Comparison of the performance of various nanostructures synthesized from MOF precursors as negative materials for lithium ion batteries.

Materials	Doping	Original MOF	Pore size (nm)	Mass normalized current (mA g^{-1})	Reversible capacity (mAh g^{-1})	Cycle numbers	Reference
Carbon	Nitrogen	ZIF-8	2	100	2132	50	[44]
ZnO(QD)@C	–	MOF-5	35	75	1200	50	[46]
Hollow ZnO@C	–	MOF-5	–	100	750	100	[48]
Co–ZnO@C	Cobalt	MOF-5	–	100	725	50	[49]
ZnO@C	–	$Zn_3(HCOO)_6$	30	100	955	50	[50]
ZnO/MWCNTs		ZIF-8	3.8–14.4	200	419.8	100	[51]
ZnO/$ZnFe_2O_4$/C	–	MOF-5	7	500	1060	60	[52]
ZnO/$ZnFe_2O_4$	–	ZnFe Prussian blue analogue	–	200	704	200	[53]
$ZnCo_2O_4$	Zinc	MOF-74	~18	100	1243	80	[54]
Co_3O_4 nanorings	–	Co-NTCDA Co-PTCDA	–	100	1370	30	[55]
Co_3O_4/3D nickel foam	–	ZIF-67	–	5000	976	500	[56]
CoSe@carbon nanoboxes	Selenium	ZIF-67	2–20	100	660	100	[57]
CoS_2 hollow prisms	Sulfur	ZIF-67	2–10	1000	737	200	[58]
FeS_2 @S-doped C	Sulfur	MIL-88-Fe	3–10	100	1336.5	200	[59]
NiP_2@C	Phosphorus	Ni-MOF-74	4–30	50	656	50	[63]
SnO_2@C	Tin (Sn)	Cu-BTC	100	100	880	200	[64]
CuO/3D graphene network	–	Cu-BTC	16	100	409	50	[65]
CuO	–	Cu-BTC	–	100	470	100	[66]
Anatase TiO_2	–	MIL-125	~1.25	10,000	127	1100	[67]
Anatase TiO_2	–	MIL-125	~1.9	1000	166	500	[68]

calcination [55]. The enhanced lithium storage performance (1370 mAh g^{-1} reversible capacity at a mass normalized current of 100 mA g^{-1}) of the obtained material has proven that the synthesis method was feasible for the preparation and modulation of metal oxides and their morphology. Besides that, the electrical conductivity of Co_3O_4 can also be improved by coating the metal oxides on electro-conductive substrates. This has been demonstrated by Fang's group, who coated porous Co_3O_4 on three-dimensional nickel foam to optimize its structural and mechanical properties [56]. A schematic illustration of the synthesis process and SEM images of the material is shown in Fig. 12. The as-synthesized material sustained a reversible capacity of 976 mAh g^{-1} at a high mass normalized current of 5000 mA g^{-1} for 500 cycles, putting this material as one of the negative electrode materials with superior cyclic stability reported in the literatures. Moreover, aside from coating porous Co_3O_4 on conductive substrates, the electrical conductivity and structural stability can also be improved by confining the particles within a hollow carbon-enriched outer shell. In 2016, Hu and co-workers pyrolyzed Se-doped ZIF-67 to obtain CoSe nanoparticles confined within hollow carbon shell [57]. Benefiting from the structural protection and pathways for charge transport provided by the hollow carbon matrix, the as-synthesized CoSe@C showed excellent cyclability by retaining a 91.6% discharge capacity (660 mAh g^{-1}) after 100 cycles at a mass normalized current of 100 mA g^{-1}. On the other hand, Yu's group had employed an ion-exchange method to convert ZIF-67 MOF into CoS_2 hollow prisms [58]. They first developed a fast ion-exchange method to produce ZIF-67 hollow prisms, followed by a sulfidation reaction to convert ZIF-67 into CoS_4 bubble-like particles. A subsequent thermal treatment then produced crystalline hierarchical CoS_2 prisms with multilevel hollow interiors. The unique structural features of hollow interior and ultrathin shells had allowed the as-synthesized nanoparticles to perform remarkably as negative electrode material for LIB with high rate capability and long-term cycling stability (reversible capacity of 737 mAh g^{-1} after 200 cycles at a mass normalized current of 1000 mA g^{-1}).

In 2016, Fe-based and Ni-based MOFs were used to fabricate derivatives of porous nanostructures for high performance LIBs. Pang and co-workers synthesized FeS_2@S-doped C from MIL-88-Fe and sulfur powder [59]. The as-synthesized material had a rice skeleton which was mainly inherited from the templating effect of the rice-like Fe-MOF precursor. This rice-like morphology was also said to be roughly maintained at a MIL-88-Fe to S powder mass ratio of 1: 2.5, in which over-sulfurization will destroy its morphology. Benefiting from the MOF derived heterogeneous porous structure as well as the sulfur-doped carbon of this composite,

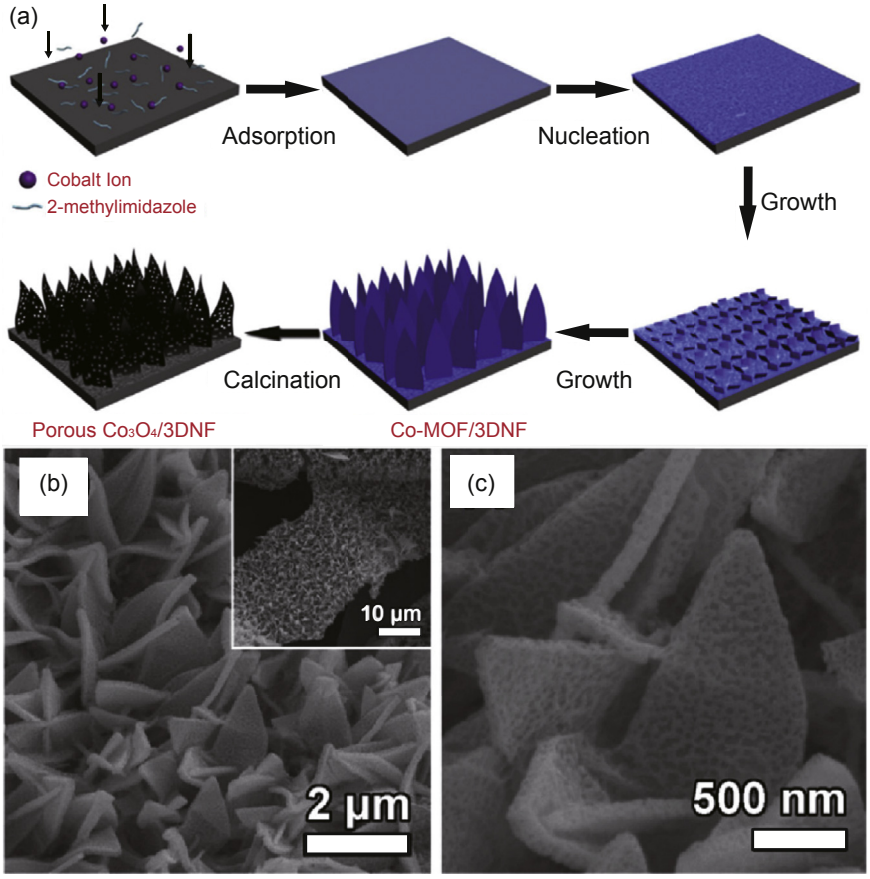

Fig. 12. (a) Schematic illustration of synthetic process of Co_3O_4/3D nickel foam hybrid, (b–c) SEM images of Co_3O_4/3DNF grown for 1 h. Reproduced from Ref. [56], with permission from Elsevier.

the FeS_2@S-doped C had achieved a large reversible capacity of 1336.5 mAh g^{-1} after 200 cycles, which was more superior than other FeS_2-based materials such as those reported in Ref [60–62]. In contrast, Li's group prepared nanostructured NiP_2@C via calcination of Ni-based MOF-74 with phosphorus [63]. The use of a MOF had retained the porous structures of the composite, whereas the introduction of porous carbon round the NiP_2 nanoparticles had greatly enhanced the electronic conductivity and stopped nanoparticles coalescence from Ostwald ripening. As a result, a reversible capacity of 656 mAh g^{-1} after 50 cycles at the mass normalized current of 50 mA g^{-1} was reported. Lastly, other examples of MOF-derived metal oxides which exhibited some electrochemical properties are SnO_2@C (from Cu-BTC) [64], CuO octahedral on 3-D graphene (from Cu-BTC) [65], CuO octahedral (from Cu-BTC) [66], and porous anatase TiO_2 (Ti-MIL-125) [67,68]. All the examples discussed in this section and their electrochemical measurements are tabulated in Table 2 and graphically presented in Fig. 13.

In summary, these MOF-derived nanostructures demonstrated high reversible capacities, rate capabilities, and cycling stabilities more superior, or at least comparable with graphite (specific capacity = 372 mAh g^{-1} [69]), the commercial negative electrode material. The most widely studied nanostructures are MOF-derived zinc oxides. However, the highest reversible capacity was achieved by MOF-derived cobalt oxides. Overall, this two-step MOF-derived method is also cost effective, convenient, and can be extended to the fabrication of other porous metal oxides with defined structures for other applications other than energy storage. Currently, improvements in terms of durability and energy density of LIBs are still very much needed. These improvements are expected to be done through more modifications of coating and doping. Lastly, while all the aforementioned examples in this section are centered on their performance as negative electrode materials for LIBs, it is also worth mentioning that MOF-derived nanostructures could also be used as positive electrode materials for lithium sulfur batteries [70,71], lithium-oxygen batteries [72,73], and lithium-selenium batteries [74].

3. Applications of MOF-derived nanostructures in catalysis

In order to meet stricter environmental standards, the chemical industry is always interested in the development of chemical processes that produce the least amount of chemical waste. In principle, catalysts with good activity and selectivity will help to increase the productivity and reduce the chemical waste produced. Therefore in the chemical industry, catalysis study is an important tool and will continue to be a key for the development of sustainable chemical processes [75]. Although homogeneous catalysts have been successfully applied in many industrial processes [76], however, they still suffer from several intrinsic drawbacks of homogenous catalysts, such as difficulty in recovery of the catalysts from the reaction mixtures and poor thermal stability of the catalysts. In comparison, heterogeneous catalysts offers the advantages of longer catalyst life, easier separation, and more efficient recycling, thus allowing energy conservations and an improved overall handling and process control [77]. As a rapidly developing class of porous materials, MOFs have continued to show their potential applications in the field of heterogeneous catalysis. The catalytic applications of the direct use of MOFs for a variety of organic reactions, photocatalysis, and tandem reactions have been reviewed comprehensively in Ref [78–80]. In addition to their applications in electrochemical energy storage (cf. Section 2.0), nanostructures prepared from calcination or pyrolysis of MOFs can also be used as chemical catalysts. Conventional synthesis methods of chemical heterogeneous catalysts, such as solvothermal, hydrothermal, and wet-impregnation methods, are challenging in obtaining catalysts with uniform active sites and surface areas [81]. Therefore, facile alternatives for new/improved catalyst compound with better long-term stability and better pore size control are of research interest. When compared to porous materials synthesized from conventional methods, MOF-derived nanostructures generally have improved catalytic activities and selectivities due to their larger surface areas (with well-defined and interconnected pore system) and facilely

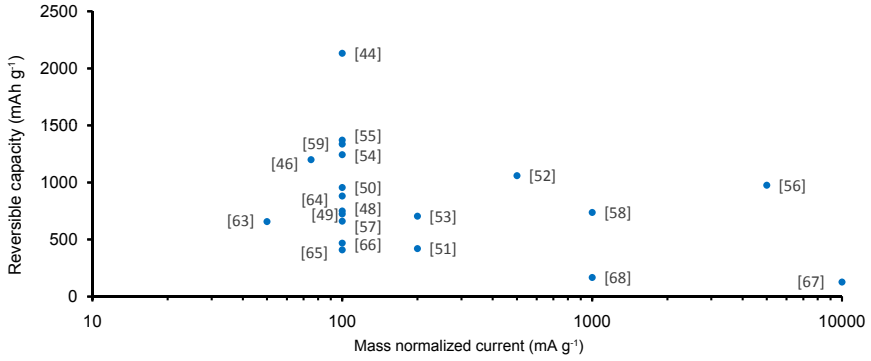

Fig. 13. Comparison of the performance of various nanostructures synthesized from MOF precursors as negative materials for lithium ion batteries [denoted by their reference number].

tailored functionality [12]. The following sections will present the recent developments of MOFs as precursors for the preparation of various functional materials, such as metal and metal oxides, in heterogeneous catalysis applications, including electrocatalysis, photocatalysis, and for the production of fine chemicals.

3.1. Electrocatalysts

Electrocatalysts shape the future of sustainable energy technologies by enhancing the rates of electrochemical reactions, such as oxygen reduction reaction (ORR), oxygen evolution reaction (OER), and hydrogen evolution reaction (HER) that take place on the surface of electrodes. Their respective half-equations are shown in Fig. 14. Due to the high cost of platinum metal, researchers are interested in developing low cost non-precious metal (NPM) catalysts that could match the performance of commercial platinum-based catalysts in terms of stability and activity. Some examples of NPM catalysts that have been studied include metal oxides, carbon materials (graphene, nanotubes, N-doped carbon), carbides and borides [82].

Meanwhile, MOFs (as precursors) have been proved to be suitable in derivation of highly active NPM electrocatalysts [86–88]. Some the earlier works which motivated researchers to develop MOF-derived metal/metal oxide-carbon nanohybrids for electrocatalysis was carried out by Chaikittisilp and his team in 2014 [89]. Their works included the synthesis of ZIF-9 derived Co_3O_4/C hybrid that has shown similar catalytic activity in ORR in comparison to the commercial Pt/C catalyst. Since then, there has been many works reported on Co-MOF derived electrocatalysts. Xia's group synthesized ZIF-67 of various crystalline sizes ranging from 300 nm to a few μm and studied the effect of crystalline sizes on the preparation of Co@N-doped carbon polyhedrons and their ORR activities and stabilities [90]. After pyrolysis under argon gas flow for 2 h (at a temperature of 750 °C), the Co@N-doped carbon polyhedrons prepared from the smallest MOF crystals exhibited the highest ORR activity. The ORR onset and half-wave potential values obtained were 0.86 V and 0.71 V vs. RHE, respectively. The protective carbon shells around the cobalt nanoparticles has successfully increased the stability of the electrocatalyst, one that is even superior to that of Pt/C in an acidic medium. The commercial Pt/C catalyst has suffered from a drastic current loss of approximately 87% after 15,000 s, whereas the as-synthesized Co@N-doped carbon catalyst exhibited only a lower attenuation of 58%. The team has then improved the preparation method to synthesize a novel Co–Co_3O_4@C mixed metal oxide nanoparticles encapsulated in a highly ordered porous carbon matrix [91]. When coated on glassy carbon (GC) electrode, these highly dispersed nanoparticles (diameter of 15–30 nm) recorded an increased onset potential of 0.93 V and half-wave potential of 0.81 V vs. RHE in ORR.

Recently, bimetallic MOF structures were used to prepare ORR electrocatalysts with a low catalyst loading and high catalytic activity. You and co-workers reported the synthesis of a Co–N–C polyhedron electrocatalyst by direct pyrolysis of Zn–Co bimetallic MOF without any post treatment [92]. An illustration of the carbonization of Zn–Co bi-MOF is shown in Fig. 15. At optimum conditions, an excellent onset potential of 0.98 V (almost comparable to the 0.982 V of Pt/C) and a half-wave potential of 0.871 V vs. RHE were obtained. Overall, the synthesized structure had well dispersed Co nanoparticles (~9.5 nm) with excellent catalyst stability and comparable ORR activity than commercial Pt/C tested in the same study.

Shang and co-workers reported a synthesis method for Co,N-doped carbon which is slightly complicated but effective in increasing the activity of the as-synthesized electrocatalysts [93]. They coated Zn–Co bimetallic ZIF nanoparticles with mesoporous silica, followed by pyrolysis at a temperature of 900 °C, and removal of the silica shell by wet chemical etching. The coating of mesoporous silica had offered protection to the Co,N-doped carbon nanoframework by preventing their irreversible fusion and aggregation during high temperature pyrolysis. The optimal as-synthesized material showed that it had a superior ORR catalytic activity performance (a onset potential value of 0.88 V vs. RHE) as compared to commercial Pt/C of the same loading in alkali media reported in the same study.

There are some reported application of metal phosphates and mixed metal oxides as electrocatalysts for OER. A facile

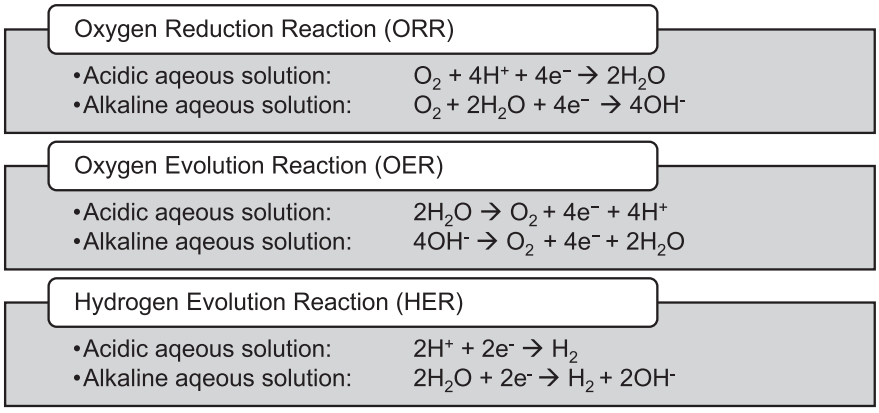

Fig. 14. Half-reactions for the water splitting reaction: ORR [83], OER [84], and HER [85] respectively.

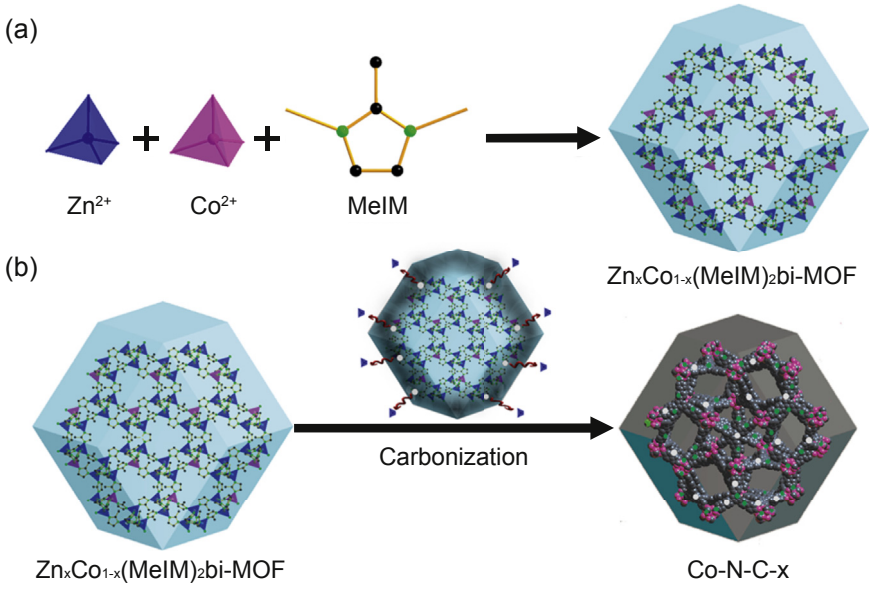

Fig. 15. Illustration of carbonization of the Zn/Co bi-MOF to produce Co–N–C. Reproduced from Ref. [92], with permission from American Chemical Society.

strategy was employed by He's team to synthesize Ni–Co–P/C nanoboxes by chemical treatment of ZIF-67 with $Ni(NO_3)_2$ and annealed with NaH_2PO_2 under nitrogen gas flow [94]. This phosphidation approach has yielded a Ni–Co–P/C catalyst with superior OER activity (with an onset potential of 1.56 V vs. RHE). This is comparable to the performance of other metal-phosphate-based catalysts such as Mn–Co–P (1.56 V vs. RHE) [95], Co–P/reduced graphene oxide (rGO) (1.57 V vs. RHE) [96], and Ni_2P (1.52 V vs. RHE) [97]. The researchers have attributed the enhanced OER performance (as compared to Ni–Co–P in the same study) to the existence of carbon which improved the charge transfer conductivity and the nanoboxes' hollow structure which presented more electrolyte/electrode contact area for the electrochemical reaction. On the other hand, Ni–Co mixed oxides nanocages were prepared by Han's group by thermally treated Ni–Co Prussian blue analogue nanocages in air [98]. The Ni–Co Prussian blue analogue was first treated with ammonia at room temperature to undergo structural evolution and transformation into a cage-like nanostructure. The complex 3D cage-like hollow and porous structure had provided a large electrolyte/electrode contact area, to which an excellent OER performance was achieved with an onset potential of 1.61 V vs. RHE.

Furthermore, nanoparticles embedded in NPC has proved its ability to function as bi-catalysts for both ORR and OER reactions. In 2015, Li's team loaded ZIF-9 derived Co_3O_4 nanoparticles onto N-doped graphitic carbon layer/MWCNT hybrid [99]. By tuning the ratio of MWCNTs to ZIF-9, the electrocatalyst has optimum ORR performance with an onset potential of 0.89 V and a half-wave potential of 0.81 V vs. RHE. Furthermore, this highly active catalyst also catalyzed OER with an onset potential of 1.50 V vs. RHE. These results have demonstrated the important role of MWCNTs in providing active sites and influencing the electron-conductive properties of the hybrid materials. In 2016, Lu and co-workers fabricated metallic Co nanoparticles embedded in NPC layers (Co@NPC) through pyrolysis of Co-BTC crystals [100]. The carbon layered structures, with a relatively uniform distribution of Co nanoparticles, exhibited a good ORR and OER bifunctional catalytic activity. For ORR, an onset potential value at 0.88 V vs. RHE was obtained. This performance was comparable to that of commercial Pt/C catalyst. As for OER, the potential value recorded was 1.61 V vs. RHE as compared to the commercial RuO_2 (1.50 V vs. RHE). Furthermore, Dong's team has adopted a similar MOF-derived approach to prepare Co-embedded NPC nanosheets [101]. They employed montmorillonite (MMT) as a template to obtain an intercalated layered structure of ZIF-67 and MMT, and subsequently removal of MMT by hydrofluoric acid etching to yield a Co-embedded porous carbon nanosheets. A schematic illustration of this synthesis strategy is shown in Fig. 16. This effective and novel strategy had produced MOF-derived nanostructures with comparable onset potential, half-wave potential, density, and durability with respect to Pt/C electrodes tested in the same study.

Similar to their applications in derivation of ORR and OER electrocatalysts, ZIF-67 and Cu-BTC can also be used as precursors to prepare promising catalysts for HER. The major challenges remain for HER electrocatalysts are low overpotential and poor stability. In 2015, Hou and co-workers pyrolyzed a mixture of graphene oxide and ZIF-67 to obtain a layered structured electrocatalyst of N-doped graphene/Co-doped C/N-doped graphene oxide [102]. The as-synthesized structures possessed excellent electrocatalytic activities for HER, OER, and ORR, with a low onset overpotential of 0.058 V vs. RHE for HER, a small onset potential of 1.66 V vs. RHE for OER, as well as a potential of 0.97 V vs. RHE for ORR. The enhanced performance of this electrocatalyst was attributed to the larger surface area, doping of nitrogen, and the presence of dual active sites provided by graphene oxide sheets.

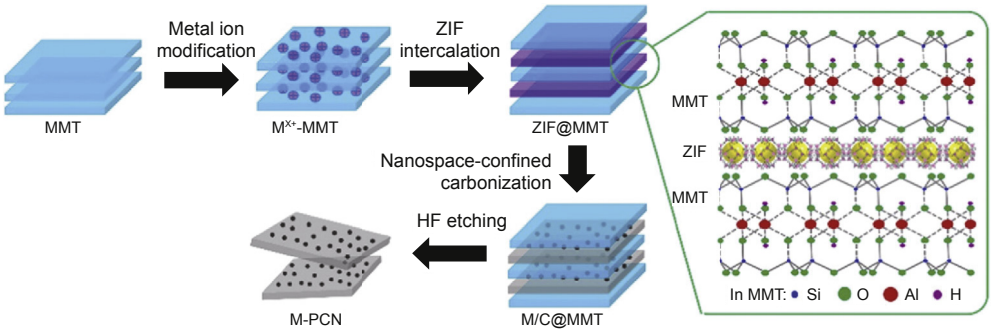

Fig. 16. Schematic illustration of the synthesis of the porous carbon nanosheets by ZIF intercalation, carbonization, followed by HF etching. Reproduced from Ref. [101], with permission from Elsevier.

The synergistic effects between various transition metal elements and the synergistic effects between these transition metals and heteroatom-doped carbon were studied by various researchers. In 2016, Chen's group developed NiCo bimetallic sulfide nanoparticles embedded in N,S-co-doped porous carbon that showed electrocatalytic activity for HER with an onset overpotential of 98 mV vs. RHE, and a current density of 10 mA cm^{-2} was achieved at an overpotential of 247 mV vs. RHE [103]. This HER performance is comparable to the most active NPM electrocatalyst reported to date. This composite catalyst also exhibited excellent activities towards the OER with an onset potential of 1.43 V vs. RHE. The researchers attributed the outstanding electrochemical performance to the uniformly distributed sulfides nanoparticles supported on high surface area carbon, the protection of core–shell carbon, and the synergistic effect between metal sulfides and S,N co-doped carbon. Also in 2016, Ming and co-workers prepared a similar CoNi bimetallic electrocatalyst (Co–Ni–Se/C@Ni foam) but with Se powder and Ni foam [104]. The team first coated ZIF-67 on Ni foam, then refluxed the sample with $Ni(NO_3)_2 \cdot 6H_2O$ before heated under nitrogen atmosphere with Se powder. When tested on the electrocatalytic performance towards HER, the as-synthesized sample needed an overpotential of merely 90 mV and 183 mV to achieve a current density of 10 mA cm^{-2} and 100 mA cm^{-2} respectively (vs. RHE). Subsequent OER performance was evaluated and an onset potential of 1.51 V vs. RHE was achieved. The sample also demonstrated good stability by showing negligible decrease in potentials after 24 h and 2000 CV cycles. The study had demonstrated the effectiveness of the co-existing of $NiSe_2$ and Ni_3Se_4 in providing more active sites, the good conductivity of the $NiSe_2/Ni_3Se_4$/C hydric nanomaterials, and the *in situ* formation of electrochemically active NiOOH phase at the surface which promoted the OER reaction. Besides that, another two research works which evaluated both OER and HER bifunctional catalytic performance using MOF-derived electrocatalysts are reported in Ref [105,106]. Yu's group fabricated Ni–P porous nanoplates through low-temperature phosphidation of Ni–Ni Prussian blue analogue [105]. The as-synthesized material delivered a current density of 10 mA cm^{-2} at a OER onset potential of 1.53 V vs. RHE, lower than that of $Ni(OH)_2$ (1.59 V vs. RHE) and NiO (1.66 V vs. RHE) obtained from Ni–Ni Prussian blue analogue in the same study. The electrocatalytic properties of Ni–P nanoplates was further investigated for HER activity in acidic solutions. An overpotential of only 110 mV vs. was required to achieve a current density of 10 mA cm^{-2}. Benefiting from this MOF-assisted synthesis method which enabled the incorporation of carbon into nickel phosphides and the presence of metallic nickel phosphides with high electrical conductivity to facilitate electron transfer. As a result, an electrocatalyst with excellent electrocatalytic activity was synthesized. The phosphidation strategy was also employed by Li and co-workers to obtain Co_2P@N,P-doped C/CNT hybrid through pyrolysis of $Co_3(PO_4)_2$ MOF and further addition of CNTs by strong sonication treatment [106]. The resultant catalysts displayed a high onset potential of 1.51 V vs. RHE for OER and an overpotential value of 0.154 V vs. RHE for the HER. This Co_2P@N,P-doped C/CNT hybrid also maintained an excellent stability of up to 25 h when used as an electrocatalyst for both anode and cathode in an overall water electrolyzer. Even though the stability was inferior to that of the well-established IrO_2/Pt couple, the study had proved the effectiveness of Co_2P for water splitting and the importance between the interaction of Co_2P and carbon structure to promote its performance as a bifunctional electrocatalyst.

Moreover, the very first work on the growth of NiFe bimetallic nanoparticles enveloped in N-doped graphene microtube for HER was demonstrated by Wu's team in the year 2017 [107]. They proved that by controlling the pyrolysis temperature, the morphologies of N-doped graphene microtubes could be tuned into bamboo-like submicro-tubes and amorphous nanotubes. Although the HER performance of these bimetallic catalysts was low as compared to the commercial Pt/C electrode, however, they exhibited the highest HER activity at an overpotential of 0.071 mV vs. saturated calomel electrode (SCE) as compared to other NiFe nanocrystals [108] and single metal HER catalyst [109] reported to date. Motivated by the feasibility to control the thickness of carbon protection shell, Zhou and co-workers developed a 3-step strategy to synthesize $CoSe_2$ bimetallic nanoparticles embedded in defective carbon nanotubes [110]. They used ZIF-8 as precursor for the growth of defective carbon nanotubes and ZIF-67 as the cobalt metal precursor. A schematic

illustration for the synthesis is demonstrated in Fig. 17. The HER activity testing revealed that the $CoSe_2$@deffective carbon nanotubes has an onset potential of −0.04 V vs. RHE. This same study has showed the importance of a core-shell structure in enhancing the stability and current density of the catalysts.

Additionally, other MOF-derived metal-carbon composite which has demonstrated electrochemical properties for HER was Cu/nanoporous carbon formed by the direct carbonization of Cu-BTC. Raoof has prepared a Cu-BTC derived Cu/C catalyst which had an overpotential of approximately −0.8 V vs. Ag|AgCl|KCl [111]. The same group also prepared bimetallic Cu−Pt@nanoporous carbon with improved electrocatalytic activity for HER with an onset potential of −0.01 V vs. RHE [112]. Their works has also proven that the synergistic effect of bimetallic nanoparticles was vital in enhancing the electrocatalytic activity of the nanomaterials.

In summary, owing to their thermal and chemical stability, ZIF family, in particular ZIF-67 and ZIF-9, were widely used as precursors for synthesis of electrocatalyst for ORR, OER, and HER. These ZIF-derived cobalt oxides exhibit superior electrocatalytic performance especially after metal doping and encapsulation by carbonaceous materials. A comparison of the performance of various nanostructures synthesized from MOF precursors as electrocatalyst for ORR, OER, and HER which were discussed in this Section 3.1 is tabulated in Table 3. Aside from the comparable onset potentials, long term stability towards, ORR, OER, and HER (especially in acidic medium) will be an important indicator in future research. Overall, the strategies which are crucial for improvement of electrocatalyst performance could be summarized as: (i) prevention of aggregation and improvement of structural stability by carbon or silica protection, (ii) presence of carbonaceous material to improve charge transfer efficiency and conductivity, (iii) nitrogen or phosphorus doping to provide additional active sites, (iv) introduction of macro/mesoporous structure with high specific surface area to provide better mass/electron transport pathways, and (v) introduction of suitable transition-metal or phosphorus to create synergistic combination which may contribute to the overall enhanced electrocatalytic activity. Lastly, to the best of our knowledge, MOF-derived nanostructures have yet to be studied as electrocatalyst for other types of reaction, such as oxidation of methanol or ethanol. This may be an interesting area of research worth exploring.

3.2. Photocatalysts

The use of solar energy to drive chemical processes such as air treatment [113], hydrogen production from water [114], carbon dioxide reduction [115], water treatment [116], and organic synthesis [117], provides an environmental friendly and alternative to traditional methods which often involve the usage of toxic chemicals, high operating cost, and generation of toxic wastes. Titanium dioxide (TiO_2) based materials are commonly used as photocatalysts. However, given that the band gap of these materials falls in the UV region, therefore, it is of paramount importance to develop photocatalysts with band gap in the visible region to maximize the utility of the solar light irradiation [118]. In general, preparation of nanoporous semiconductor-based materials for photocatalytic applications is achieved through methods such as sol−gel

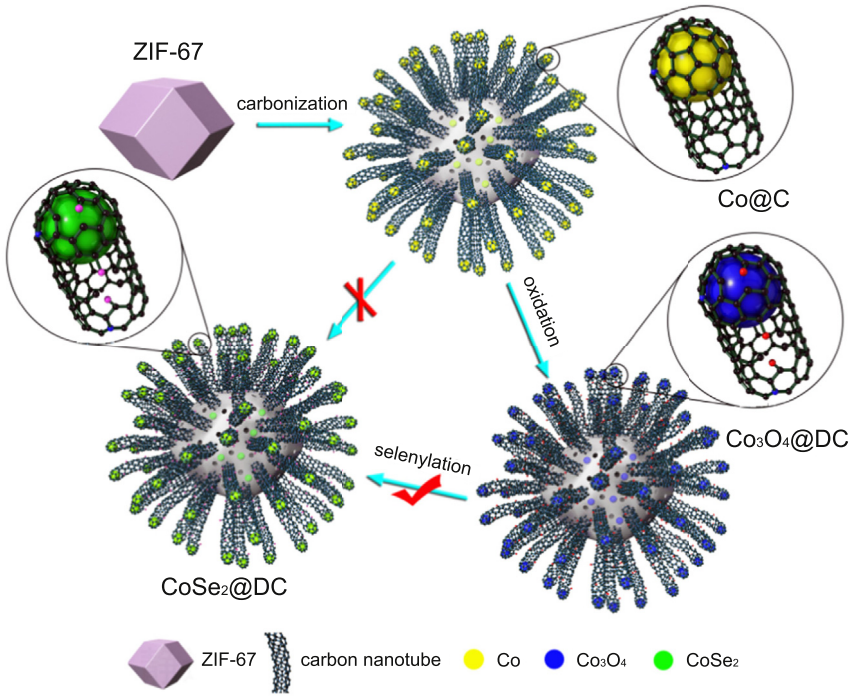

Fig. 17. Schematic illustration of the synthesis procedure for $CoSe_2$@defective carbon. Reproduced from Ref. [110], with permission from Elsevier.

Table 3
Comparison of the performance of various nanostructures synthesized from MOF precursors as electrocatalyst for ORR, OER, and HER.

Electrochemical reaction	Materials	Original MOF	Catalyst loading (mg cm^{-2})	Onset potential values (V)	Reference electrode	Electrolyte	References
ORR	Co_3O_4–C	ZIF-9	0.25	−0.05	Ag/AgCl	0.1 M KOH	[89]
ORR	Co@N-doped C polyhedron	ZIF-67	0.40	0.86	RHE	0.1 M $HClO_4$	[90]
ORR	Co–Co_3O_4–C@C matrix	ZIF-9	0.10	0.93	RHE	0.1 M KOH	[91]
ORR	Co–N–C Nano polyhedron	Zn–Co Bimetallic ZIF	0.28	0.98	RHE	0.1 M KOH	[92]
ORR	Co–N-doped C	Zn–Co Bimetallic ZIF	–	0.88	RHE	0.1 M KOH	[93]
OER	NiCoP/C	ZIF-67	–	1.56	RHE	1.0 M KOH	[94]
OER	Ni–Co Cages	Prussian Blue Analogue	–	1.61	RHE	1.0 M KOH	[98]
ORR OER	Co_3O_4@N-doped graphitic C/MWCNT hybrid	ZIF-9	0.33	0.89 1.50	RHE	0.1 M KOH 1.0 M KOH	[99]
ORR OER	Co@NPC	Co-BTC	0.40	0.88 1.61	RHE	0.1 M KOH	[100]
ORR OER	Co@NPC	ZIF-67	0.10	1.02 (0.71) 1.50	RHE	0.1 M KOH (0.5 M H_2SO_4) 0.1 M KOH	[101]
ORR OER HER	N-doped graphene/Co@/ N-doped graphene oxide	ZIF-67	0.71	0.97 1.66 Overpotential 0.058	RHE	0.1 M KOH 0.1 M KOH 0.5 M H_2SO_4	[102]
OER HER	Ni_1Co_4@N,S-doped C	ZIF-67	0.14	1.43 Overpotential 0.098	RHE	0.1 M KOH 0.5 M H_2SO_4	[103]
OER HER	Co–Ni–Se–/C@Ni Foam	ZIF-67	1.50	1.51 Overpotential 0.090	RHE	1.0 M KOH	[104]
OER HER	Ni–P Nanoplate	Ni–Ni Prussian Blue Analogue	0.20	1.53 Overpotential 0.11	RHE	1.0 M KOH 0.5 M H_2SO_4	[105]
OER HER	Co_2P@N,P-doped C/CNT hybrid	$Co_3(PO_4)_2$	0.36	1.51 Overpotential 0.154	RHE	0.1 M KOH	[106]
HER	NiFe@N-doped Graphene tube	$NiFe(CN)_5NO$ $2H_2O$	–	Overpotential 0.071	SCE	0.5 M H_2SO_4	[107]
HER	Co@N,B-doped C cages	ZIF-67	–	Overpotential 0.096	RHE	0.5 M H_2SO_4	[109]
HER	$CoSe_2$@defective C	ZIF-67	0.36	−0.04	RHE	0.5 M H_2SO_4	[110]
HER	Cu@C	Cu-BTC	–	Overpotential −0.80	Ag/AgCl/KCl	0.5 M H_2SO_4	[111]
HER	Cu–Pt@C	Cu-BTC	–	−0.01	RHE	0.5 M H_2SO_4	[112]

method, hydrothermal method, sonochemical method, spray-drying method, anodization method, and deposition method [119]. These methods focused on enhancing the catalytic performance of the photocatalysts through ligand modification, photosensitization, metal doping, modification with noble metal nanoparticles, modification with carbon materials, and coupling with semiconductors [120]. In principle, these strategies aim at increasing the accessibility of the active sites (to increase light absorption) and decreasing the recombination rate of photo-generated charge carriers.

Despite the increasing complexity of waste water, semiconductor photocatalytic processes have shown a great potential as a sustainable treatment technology in the water/wastewater industry. Among the photocatalytic materials studied (such as hydro complexes of copper, iron, and metal oxides), MOF-derived ZnO was found effective to remove organic compounds from wastewater. In 2013, Du and co-workers obtained porous ZnO powder by direct thermal treatment of ZIF-8 in air and investigated its performance on the degradation of methylene blue [121]. Despite showing better photocatalytic activity than ZIF-8 and commercial TiO_2, the catalytic evaluation of this ZnO was carried out under UV light, which only accounts for 5% of the natural light. In 2016, Pan's group employed a two-step calcination strategy to overcome the challenges in obtaining ZnO from ZIF-8. These challenges include complete removal of organic ligands and prevention of structural collapse and serious aggregation of the ZnO particles [122]. They first calcined ZIF-8 at 350 °C for 2 h, followed by 1 h calcination at 400 °C. The size, morphology, and crystallinity of the materials were controlled by tuning the calcination temperature, time, and heating rate. The photocatalytic performance of the ZnO particles was evaluated on the visible light degradation of organic dyes (rhodamine-B and phenol) and photoelectrochemical (PEC) water splitting. Their experiment has demonstrated that the two-step calcined samples has the highest photoactivity and PEC activity as compared to the one-step calcined samples. On top of that, they have also shown that high temperature

calcination has removed the C species and produced pure ZnO, whereas mild temperature calcination resulted in C doping in the ZnO crystals. The SEM images of these two-step calcined samples with different calcination time are shown in Fig. 18 where the influence of the calcination duration on ZnO structures can be observed.

Recently, the non-metal doping method was also applied to enhance the visible light harvesting ability of photocatalysts. Feng's team synthesized N-doped ZnO via direct calcination of urea and ZIF-8 mixtures at 550 °C for 3 h, and likewise evaluated the sample's performance on the degradation of organic dyes (rhodamine-B and phenol) under visible light [123]. The photocatalytic activity of N-doped ZnO in the degradation of rhodamine-B was approximately 2.5 times higher than the ZIF-8 derived pure ZnO, and a 13.2% increase in phenol degradation than that of ZIF-8 derived pure ZnO. The group attributed the enhanced photocatalytic activity of the N-doped ZnO to the presence of nitrogen in the structures which has helped to improve its visible light harvesting ability and inhibition of the recombination of photo-excited electrons and holes. Besides, Zhu and co-workers has incorporated rGO onto the ZIF-8-derived ZnO particles [124]. The introduction of rGO was speculated to be able to decrease the excitonic photoluminescence intensity and inhibit the recombination of photo-excited electrons and holes. Therefore, the amount of rGO incorporated onto the ZIF-8-derived ZnO was carefully manipulated and its visible light absorption ability in the degradation of methylene blue dye was observed. A maximum degradation efficiency of 82% was achieved with the ZnO catalyst containing 1.5 wt.% of rGO. Further increment of rGO loading has caused a decrement in the photocatalytic performance of the ZnO catalyst due to increased competition for recombination centers. These rGO-doped ZIF-8 derived ZnO catalysts also showed a stable photocatalytic activity after six successive cycles of degradation experiments.

Transition metals have also attracted attention for photocatalytic hydrogen production from water. Zhang's team reported a novel type of Co_3O_4/CuO hollow bimetallic polyhedral nanocages, derived from ZIF-67, as an efficient photocatalyst for water oxidation [125]. A maximum oxygen yield of 50% and quantum yield of 49% (normalized to per mole of transition metal) were reported. Besides that, the group proposed an alternative reaction mechanism for the light-driven water oxidation system. They speculated that the heterojunctions, formed by Co_3O_4 and CuO, could enhance charge separation by an internal electric field, which in turn lead to the enhancement of the photocatalytic activity. The overall photocatalytic water oxidation cycle is shown in Fig. 19.

In 2015, Xu and co-workers reported a magnetic $FeO_{3.3}C_{0.2}H_{1.0}$ photocatalyst prepared from *in situ* decomposition of earth abundant Fe-MOFs (MIL-101 and MIL-53) and its simultaneous hydrogen production from water [126]. Photocatalytic hydrogen evolution experiments were performed by irradiating the solution in the presence of the Fe-MOF using a white-light LED. The MOF-derived catalyst was synthesized *in situ* while hydrogen is simultaneously produced at a rate of approximately 4.17×10^3 mol h^{-1} g^{-1}. The modified composite structure was proved to have better water reduction performance than pristine MOFs [127] or MOF-supported photocatalysts [128]. Knowing that the conventional iron oxide nanoparticles cannot be used to produce hydrogen from water [126], this study has demonstrated the importance of carbon content in enhancing the activity of the photocatalysts. Furthermore, deposition of MOF-derived Ni_2P on CdS nanocrystal (Ni_2P/CdS) to obtain a compound which

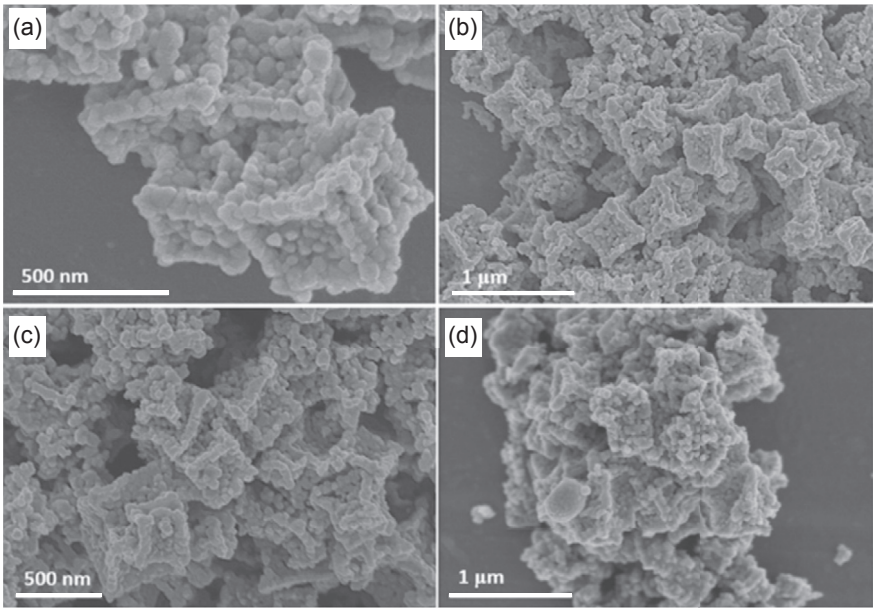

Fig. 18. SEM images of two-step calcined samples with different calcined time. (1) 350 °C for 1 h and 400 °C for 1 h; (b) 350 °C for 2 h and 400 °C for 2 h; (c) 350 °C for 2 h and 400 °C for 3 h; (d) 350 °C for 2 h and 400 °C for 4 h. Reproduced from Ref. [122], with permission from Elsevier.

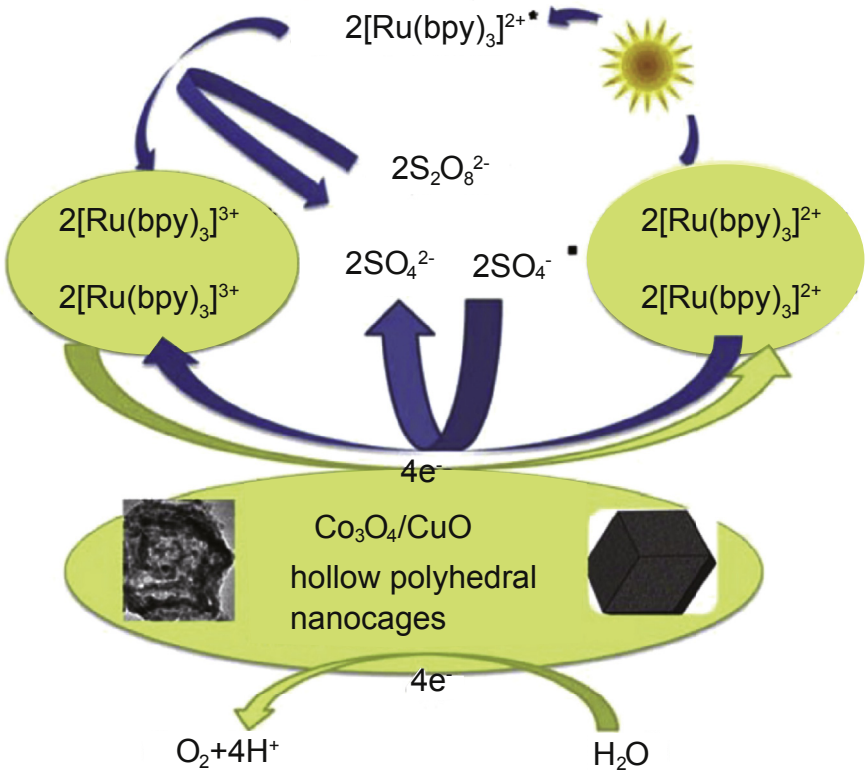

Fig. 19. Photocatalytic water oxidation cycle in the presence of catalyst, photosensitizer, and electron acceptor. Reproduced from Ref. [125], with permission from Elsevier.

exhibited efficient hydrogen production from water was demonstrated by Kumar's group in 2016 [129]. Under optimum Ni_2P on CdS loading condition (2.0 wt.% of Ni_2P loading), the rate of hydrogen production from visible-light-driven water reduction was 3.35×10^{-2} mol h^{-1} g^{-1}, putting it as one of the best catalytic results to date. The high photocatalytic activity was attributed to the fine dispersion and good electrical conductivity of the Ni_2P as well as its ability to minimize the recombination of the photo generated electrons. A plausible mechanism for efficient hydrogen production under solar irradiation using lactic acid as a hole scavenger and Ni_2P/CdS as a photocatalyst is presented by the team and depicted in Fig. 20.

Lastly, an interesting study was presented by Li and co-workers who investigated MIL-125 derived cake-like mixed phase of TiO_2 and proved that it has better photocatalytic performance than pure anatase or rutile phase TiO_2 [130]. The excellent efficiency of 97% in nitrobenzene degradation was due to the constructed structure of energy levels which effectively reduce the combination of electron–hole pairs.

3.3. Catalysts for production of fine chemicals

The fine chemical industry, such as the pharmaceutical and agrochemical industry, often require chemicals with high degree of purity. However, the production of fine chemicals are often performed in liquid phase reaction medium that contain mixtures of catalysts and complex organic molecules [131]. Therefore, it is advantageous to develop heterogeneous catalysts that can be easily isolated from the complex reaction mixtures. MOFs can be used to prepare heterogeneous catalysts for the synthesis of fine chemicals. Among MOFs, ZIFs have emerged as an ideal precursor for the preparation of metal–metal oxides/carbon heterogeneous catalysts. As a subfamily of MOFs, ZIFs are formed by the bonding of imidazole, benzimidazole or methyl-imidazole ligands with primarily zinc or cobalt metal ions. By having different organic linkers which altered the accessible bonding angle, ZIFs have magnetic properties, better thermal stability and chemical stability in organic solvents than other MOFs [132].

3.3.1. ZIF-67-derived catalysts

Yusran and co-worker synthesized Co@N-doped C (Co@N–C) through the direct carbonization of ZIF-67 under nitrogen flow for 3 h (at temperature range of 600–800 °C) without any pre-treatments [81]. This Co@N–C has a specific activity of 2.25 mol h^{-1} g^{-1} in reduction of 4-nitrophenol to 4-aminophenol in the presence of $NaBH_4$. The Co@N–C catalyst could also be magnetically separated and reused for up to six times. Li's group has prepared a similar Co@N–C nanoparticles from ZIF-67 but with a longer pyrolysis duration of 5 h [133]. The resulted Co catalyst has a lower catalytic activity of 0.313 mol h^{-1} g^{-1} for the reduction of 4-nitrophenol. However, the as-synthesized material was able to retain a conversion of over 95% even after 17 successive reaction cycles. Alternatively, Wang and Li pyrolyzed ZIF-67

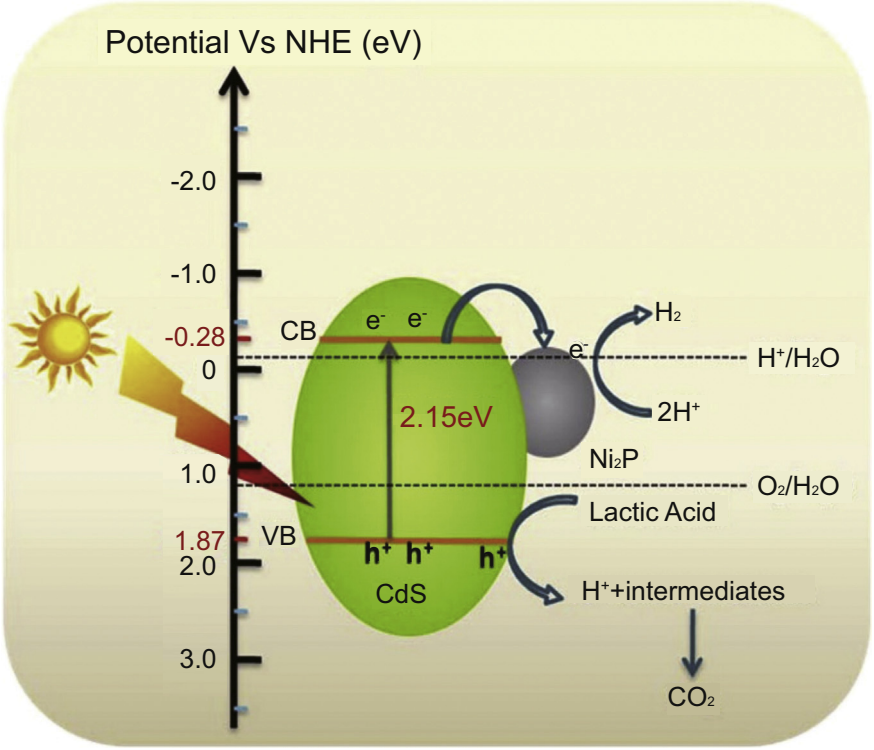

Fig. 20. Proposed reaction mechanism of Ni_2P/CdS. Reproduced from Ref. [129], with permission from American Chemical Society.

under argon atmosphere for 10 h in the temperature from 600 °C to 900 °C to yield a porous Co@N–C catalyst for the selective hydrogenation of 4-nitrostyrene to 4-aminostyrene [134]. While the pristine ZIF-67 was inactive, the pyrolyzed ZIF-67 showed a high catalytic performance with a 99% conversion and a 97% selectivity, resulting in a specific activity of 1.111×10^{-5} mol h^{-1} per mol% of Co@N–C-catalyst. The magnetically separated catalyst also showed high stability and reusability for at least five successive reaction cycles. The above three studies demonstrated the effectiveness of Co–N centers for the selective hydrogenation of nitro groups, as well as the efficiency of employing MOF-derived structures as catalyst.

Recently, Lin and co-workers synthesized a Co_3O_4 based magnetic carbonaceous nanocomposite (MCN) by pyrolysis of ZIF-67. The Co_3O_4/MCN catalyst exhibited a high catalytic activity to activate Oxone to degrade a dye pollutant - Rhodamine B in water [135], as well as able to efficiently eliminate caffeine from water [136]. By employing such simple (one-step MOF pyrolysis) preparation method, the produced materials showed excellent catalytic activity by allowing Oxone oxidation and generation of radicals [135]. A complete removal of Rhodamine B was recorded under 1 min, resulting in a catalytic activity of 0.125 mol h^{-1} g^{-1} in the presence of Oxone. On the other hand, a catalytic activity of 2.57×10^{-3} mol h^{-1} g^{-1} was achieved for the removal of caffeine from water. Recyclability test for both studies also revealed that these nanocomposites can be used continuously for three successive reaction cycles while retaining more than 95% of the catalytic activity. A schematic illustration of MCN synthesis and its activation of Oxone, and SEM images of ZIF-67 and MCN respectively are shown in Fig. 21.

Besides that, some other reports on ZIF-67 as precursors to form heterogeneous catalyst for various reactions includes aerobic oxidation of alcohols [137,138], aerobic oxidation of cyclohexane [139], and aerobic epoxidation of styrene [140]. The use of MOF-derived nanostructures for liquid-phase catalytic oxidation reactions are scarce. Studies reported by Ref [137,138] made breakthroughs when their Co@N–C catalyst observed excellent conversion and selectivity with a broad substrate scope for both aromatic and aliphatic alcohols under atmospheric pressure reaction. These two groups of researchers have attributed the enhanced catalytic performances to the interaction of nitrogen-carbon (which allowed the uniform dispersion of Co nanoparticles) and nitrogen doping (which promoted basic properties of the catalysts). Excellent catalytic results were also demonstrated by Wang and Li, who derived metal-free NPC from ZIF-67 for the aerobic oxidation of cyclohexane [139]. The as-synthesized materials showed 48% cyclohexane conversion with a 61% selectivity to adipic acid. The NPC catalyst also reported a catalytic activity of 8.69×10^{-2} mol h^{-1} g^{-1} and a reusability for five successive cycles. Lastly, conventional epoxidations of styrene are usually performed with homogeneous transition metal complexes and hazardous oxidants [141]. However, Yu and co-workers achieved a 91.3% styrene conversion and a 84.8% epoxide selectivity by using a recyclable, inexpensive ZIF-67-derived Co@N–C heterogeneous catalyst and an eco-friendly oxidant (air) [140]. This Co@N–C catalyst also had better conversion and comparable selectivity to other Co-based

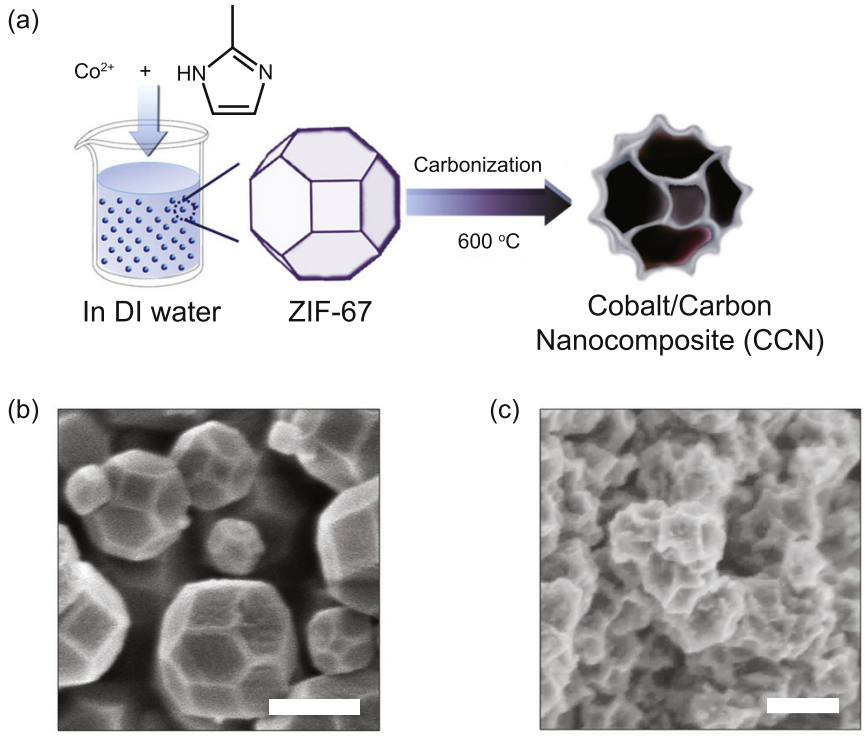

Fig. 21. Synthesis and morphology of ZIF-67 and MCN: (a) schematic illustration of CCN synthesis; (b) and (c) are the SEM images of ZIF-67 and CCN respectively (the scale bar is 500 nm). Reproduced from Ref. [136], with permission from the Royal Society of Chemistry.

heterogeneous catalysts such as those reported in Ref [142,143]. Overall, the novel Co-MOF derived catalytic system holds multiple advantages including facile magnetic separation of the catalyst, environmental friendliness, and excellent product selectivity.

3.3.2. ZIF-8-derived catalyst

Two groups of researchers have studied the catalytic performance of ZIF-8 derived NPC materials in hydrochlorination of acetylene. Li and co-workers carbonized ZIF-8 under nitrogen flow at 950 °C for 5 h and manipulated the amount of melamine species (nitrogen source) to observe the hydrochlorination performance of those samples [144]. The highest 60% acetylene conversion was achieved under optimal conditions, with a catalytic activity of 2.123×10^{-3} mol h^{-1} ml^{-1}. Meanwhile, Chao and co-workers obtained NPC by carbonizing ZIF-8 under NH_3 flow at different temperatures (600−1100 °C) for 5 h [145]. They observed a remarkable acetylene conversion and vinyl chloride selectivity of 92% and 100%, respectively. The activity of NPC catalyst remained stable for more than 200 h until it experienced deactivation due to coke deposition on active sites offered by pyridinic N from N-doping. Researchers from the aforementioned studies had provided similar conclusion, of which nitrogen content improves the performance of the catalyst by displaying microcrystalline structures but increasing the N amount (beyond optimum) will lead to an increase in coke deposition and thus leading to catalyst deactivation.

3.3.3. Cu-BTC-derived catalyst

Cu-BTC is also an ideal candidate for the preparation of various metal/metal oxide/carbon hybrids. In 2016, Zhang's group prepared Cu/CuO/C nanocomposites from the direct carbonization of Cu-BTC and studied its catalytic effect on CO oxidation [146]. By careful control of the annealing temperature and heating rate, the as-synthesized carbon encapsulated Cu/Cu_2O catalysts achieved a complete CO conversion (1 vol.%) at a reaction temperature of 155 °C and maintained its stability up to 40 h. The team had found out that the optimum annealing temperature for the preparation of catalyst is approximately 500 °C. Calcination temperatures below 500 °C will cause poor crystallinity whereas higher temperatures will lead to serious agglomeration of the catalyst particles. In contrast, Niu's group synthesized the same carbon supported Cu/Cu_2O composites from Cu-BTC for the catalytic reduction of 4-nitrophenol [147]. Despite the usage of an additional phenol formaldehyde resin as carbon precursor, the synthesized highly dispersed nanoparticles demonstrated 100% 4-nitrophenol conversion with an excellent catalytic activity (0.281 mol h^{-1} g^{-1}) which was superior than other noble metal and copper based catalysts reported in Ref [148,149]. In addition, heterogeneous Cu@C catalyst generated by the pyrolysis of Cu-BTC was also carried out by Kim and co-workers to study its catalytic performance the synthesis of N-sulfonyl amidine via a three-component coupling reaction [150]. With the help of CH_3CN as solvent, the researchers found that 5 mol.% of Cu@C could achieved a 92% yield under 3 h. The Cu@C catalyst also maintained its stability by

showing no significant decrement in catalytic activity after 4 successive reaction cycles.

Doping of Cu with other types of metal is a useful strategy to enhance its catalytic ability. In 2016, Qin and co-workers loaded HKUST-1 with Sr, La, Ce, and Al atoms, pyrolyzed the mixtures in nitrogen atmosphere at a temperature of 600 °C for 3 h, and then studied the effects of different metal doping on NO reduction reaction [151]. The SEM images of these MOF structures before and after pyrolysis are shown in Fig. 22. It was found that Sr, La, Ce, and Al doping increased the number of activated Cu^{+} sites, hence improved the overall catalytic performance as compared to the original Cu-BTC material. Equally effective, nickel-doped Cu@C catalyst derived from Cu-BTC was prepared by Wang's team for the conversion of furfural to cyclopentanone [152]. The addition of Ni led to CuNi bimetallic interaction which dramatically increased the catalyst's activity and selectivity to achieve a 99.3% conversion of furfural and a 96.9% yield of cyclopentanone (with a catalytic activity of 0.103 mol h^{-1} g^{-1}). However, a further increased (beyond optimum Ni Cu molar ratio of 0.5:1) in Ni loading caused a sharp fall in yield because high loading of Ni led to the collapse of the MOF structures and subsequently a reduction in surface area and pore volume.

3.3.4. Other MOF-derived catalyst

On the side note, other less common but equally effective MOF-derived nanocatalysts includes Fe_3O_4@C (from Fe-BDC) for the oxidation of various alcohols [153] and Cu@C (from Cu-BDC) for the synthesis of propargylamines [154]. In 2016, Yao and co-workers synthesized highly efficient and reusable magnetic heterogeneous Fe_3O_4@C catalyst which could achieve a 99% benzyl alcohol conversion with a 91% selectivity to benzaldehyde after 48 h reaction time [153]. The as-synthesized catalyst could be easily separated and was tested for four successive reaction cycles without significant loss in catalytic efficiency. In 2017, Cheng's group deposited Cu nanoparticles on Zn-BDC derived porous carbon and studied its catalytic performance for the synthesis of propargylamines in a three-component coupling reaction [154]. The hierarchical pores of MOF-derived carbon and its synergetic interaction with Cu nanoparticles had brought about a 96% product yield with just the use of 20 mg of Cu@C catalyst. Furthermore, Ni-BDC were used to prepare Ni@NPC for the oxidation of ethylbenzene to acetophenone by Zhou and co-workers in 2016 [155]. With the addition of 2.5×10^{-3} mol of *tert*-butyl hydroperoxide, a conversion and selectivity of both more than 99% were achieved within 48 h of reaction time. Even though a low catalytic activity of 0.208 mol h^{-1} mol^{-1} of Ni catalyst was reported, yet, the study is a step forward for the development of cost-effective heterogeneous selective oxidation of alkanes. Besides that, a bifunctional Cu^{2+} doped CeO_2 catalyst, from the pyrolysis of Cu-doped Ce-BTC MOF, was synthesized for CO oxidation and selective NO reduction [156]. The catalytic activity was found to be dependent on the doping of Cu^{2+} into the CeO_2 lattice (enormous Cu−Ce−O linkages which facilitated the adsorption of CO) and is proportional to the increased in the surface area. The stability of the as-synthesized material was demonstrated by retaining 100% conversion of CO to CO_2 even after five successive reaction cycles. Although high temperatures (above 380 °C) are required for the complete conversion of NO to N_2, the catalytic process is free of corrosive and organic gases.

In summary, this section demonstrates that nanostructures derived from various MOFs can be used as catalyst (with excellent conversion and selectivity) for various fine chemical synthesis reactions such as hydrogenation of 4-nitrostyrene, aerobic oxidation of alcohols, hydrochlorination of acetylene, oxidation of CO, and so on. It is also worth noting that MOF-derived nanostructures can also catalyzed the production of bulk chemicals like those reported in Ref [157]. The pore structure and functions of these MOF-derived catalysts can be tailored made by modification of the functional groups present in the pristine MOFs. Without the use of hard-templates or tedious preparation procedures, MOF-derived nanostructures demonstrate enhanced catalytic performances than those materials prepared from other synthesis methods such as impregnation. The catalytic performances of these MOF-derived nanostructures can also be tuned further through careful controlling of the pyrolysis/calcination temperature, heating time, and heating rate. However, the catalysts derived from MOFs suffered from some drawbacks, such as low surface areas, low hydrolytic stability and relatively low production capacity. These problems will need to be overcome before the commercialization of these MOF-derived catalysts.

4. Applications of MOF-derived nanostructures in sensing

Recently, the synthesis of metal oxide nanocomposites and carbon nanomaterials for gas sensing applications has gained some research interests. According to a review done by

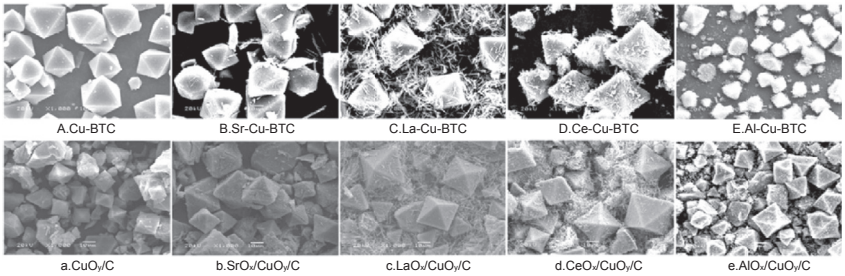

Fig. 22. SEM images of A-Cu-BTC and $AO_x/CuO_y/C$, where A = Sr, La, Ce, Al. Reproduced from Ref. [151], with permission from Elsevier.

Kumar's group, the precise control of composition and the use of most appropriate technologies for the reproducible fabrication of nanocomposites are crucial for the development of gas sensors [158]. Meanwhile, the unique properties of MOF structures have motivated their active research for potential application in gas sensing, bio-sensing, and chemo-sensing [159]. Aside from its direct use, MOFs have also been used as precursors/sacrificial templates for the synthesis of MOF-derived nanostructures for sensing purposes.

In 2016, Li and co-workers constructed hollow ZnO nanocages from thermal decomposition of MOF-5 [160]. Using a controlled slow heating rate of 1 °C/min, the ZnO nanocages produced had a cavity diameter of approximately 60 nm and a porous shell thickness of approximately 25 nm. In comparison with other ZnO nanoparticles, the as-synthesized hollow ZnO nanocages showed significantly enhanced chemical sensing sensitivity towards acetone and benzene, with a good selectivity towards acetone. The study revealed that MOF-derived hollow nanocages structure had successfully facilitated the diffusion and surface reaction of gas molecules by providing more surface oxygen vacancies due to their more exposed active sites and larger specific surface area. The team then improved their synthesis procedures to construct core–shell Au@ZnO nanoparticles derived from Au-MOF and focused on the performance of acetone gas-sensing [161]. The researchers attributed the enhanced performance to the electronic and chemical sensitization of gold particles. Schematic illustration of the energy band diagram of Au@ZnO nanoparticles and the redox process between acetone molecule and active oxygen species is shown in Fig. 23.

Another notable example of metal oxide which demonstrated sensing ability was Co_3O_4. Its advantages as gas sensing materials were reviewed by Xu and Cheng in 2016 [162]. In the same year, Qu's team prepared non-spherical Co_3O_4/$NiCo_2O_4$ double-shelled nanocages by direct annealing of ZIF-67 [163]. The as-synthesized materials exhibited enhanced gas detection sensitivity and excellent selectivity to acetone when compared with Co_3O_4 nanocages. The enhancement was attributed to the synergistic effect exerted by Co_3O_4 and $NiCo_2O_4$ and the change of heterojunction barrier at different gas atmospheres.

In 2014, Tan and co-workers fabricated Cu@C nanoparticles through one-step pyrolysis of Cu-BTC and were the very first few to begin studying the application of MOF-derived nanostructures in biomedical fields [164]. Characterizations of the Cu@C proved that the copper nanoparticles had no changes in morphology after heat-treated at 400 °C for 2 h under nitrogen atmosphere. The strategy is deemed effective because copper agglomeration is a common concern. After discovering its excellent exhibition of intrinsic peroxidase-like activity and ability to catalyze the oxidation of 3,3′,5,5′-tetramethylbenzidine (TMB) by H_2O_2, the team later designed a colorimetric method for the detection of ascorbic acid. This simple and low cost detection method was useful for the analysis of ascorbic acid content in tablets and gave the opportunity for MOF-derived nanoparticles to be applied in bioanalysis. In 2016, Tan worked with another group of researchers to fabricate magnetic porous carbon nanocomposite derived from iron-containing MOF (MIL-88A) and proved its feasibility for DNA detection [165]. They built a magnetic porous carbon-based fluorescent sensing which abled to measure accurately the levels of DNA in fetal bovine serum samples. The MOF-derived porous carbon exhibited excellent selectivity to specific target DNA and had high sensitivity with a detection limit of 1 nano-molar.

Overall, these studies further expand the application of MOF-derived nanostructures into the field of sensing. Although not as much attention is given to sensing applications as compared to energy storage and catalysis, yet this is a field that should not be neglected. The next section will include some discussion on other less established applications that had been explored so far.

5. Other applications

With the advancement of technologies and increasing number of industrial facilities, wastewater pollution is a growing environmental concern. The presence of commercial azo dyes, antibiotics, metal ions, and pharmaceutical drugs in wastewater streams are worrying because they may cause adverse effects to the environment, human health, and aquatic lives. Among the various established technologies and

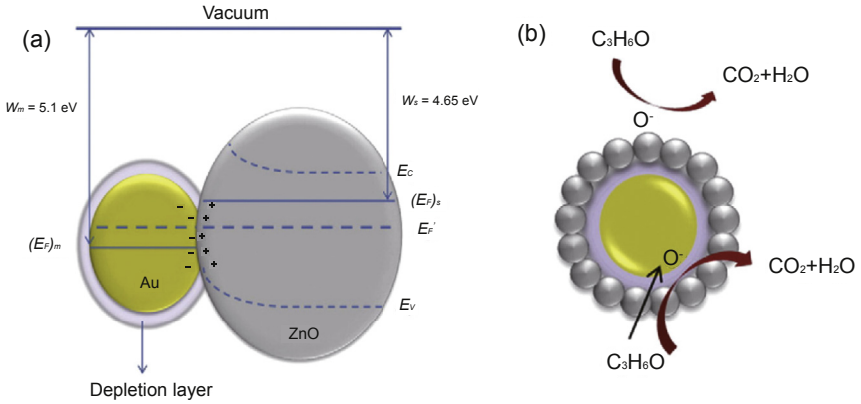

Fig. 23. Schematic illustration of (a) energy band diagram of core–shell Au@ZnO nanoparticle; (b) redox process between acetone molecule and active oxygen species. Reproduced from Ref. [161], with permission from Elsevier.

methods proposed for wastewater treatment, such as phase separation, oxidation, coagulation, etc., the adsorption method is considered a better alternative because of its design simplicity and ease of operation [166].

Recently, adsorption using ordered carbonaceous materials prepared from MOF precursors has emerged as a new innovative strategy. Researchers have found that nanoporous carbon synthesized by the direct carbonization of ZIF-8 can be used as an efficient and recyclable adsorbent for the removal of contaminants from water. The contaminants which were successfully removed from water using ZIF-8 derived nanoporous carbon includes: ibuprofen and diclofenac anti-inflammatory drugs [167], sulfamethoxazole antibiotics [168], ciprofloxacin antibiotics [169], copper ions from aqueous solution [170], and benzoylurea insecticides [171]. Although a clear understanding of adsorption mechanism has not been reached, but the removal of ibuprofen and diclofenac anti-inflammatory drugs from water via liquid-phase adsorption is a new step forward. That is especially novel when the as-synthesized MOF-derived porous carbon has better adsorption capacity (320 mg g^{-1}) than commercial activated carbon (105 mg g^{-1}), which is well known for its porosity [167]. For the removal of sulfamethoxazole and ciprofloxacin antibiotics (both used for the treatment of bacterial infections), both Ahmed's and Li's research groups had found that pyrolysis temperature has a significant impact on the porosity and adsorptive capacity of the ZIF-8 derived carbon materials [168,169]. While the optimized pyrolysis temperature for the removal of sulfamethoxazole is at 1000 °C, the removal of ciprofloxacin was best achieved with a pyrolysis temperature of 700 °C. Notably, both studies reported better adsorption capacity than other material reported in their field to date. The obtained sulfamethoxazole adsorption capacity (435 mg g^{-1}) was higher than wood-based activated carbon (329 mg g^{-1}) [172] and commercially available activated carbon (118 mg g^{-1}) [173]. Meanwhile, the obtained ciprofloxacin adsorption capacity (417 mg g^{-1}) was higher than those obtained from graphene oxide (379 mg g^{-1}) [174], microporous activated carbon (131 mg g^{-1}) [175], and MWCNTs (206 mg g^{-1}) [176] reported to date. Furthermore, the ZIF-8 derived nanoporous carbon fabricated by Bakhtiari and co-workers also proved to have at least five times higher removal percentage compared to other different activated carbon materials (including carbon cloth, granular activated carbon, powdered activated carbon and nitrogen-containing activated carbon), for the removal of heavy metal copper ions from aqueous solution [170]. That is because the fast-molecular diffusion of copper ions was facilitated by the slightly lower surface area but much higher pore volume and smaller average pore size of MOF-derived carbon as compared to other carbonaceous adsorbents. In addition, the solid phase extraction adsorption of benzoylurea insecticides was successfully carried out by ZIF-8 derived nanoporous carbon, synthesized by Liu's team [171]. The porous carbon catalyst demonstrated efficient adsorption capacity (at concentration range 0.5–100 ng mL^{-1}), rapid uptake (15 min), and facile recyclability (at least 30 times), thus proving its potential as a new adsorbent for organic pollutants from various kinds of samples.

The doping of metal on MOF-derived nanoporous carbon is also useful to broaden the application for wastewater treatment. In 2016, Cui and co-workers studied the removal of chlorophenols pollutants through hydrochlorination by using Pd@NPC (NPC derived from Ni-BTC) [177]. The as-synthesized materials demonstrated high catalytic activity in liquid phase hydrochlorination reaction and showed good magnetic recycling properties (recycled up to 5 times). The MOF-derived synthesis approach allowed the production of magnetic porous carbon materials which is important for efficient recycling of precious metal like Pd. On the other hand, Cu_2O/Cu/C from Cu-BTC was reported for catalytic decoloration of commercial azo dye [178]. As an effective catalyst at a dose of 0.11 g/L, it completely decolorized methylene blue, rhodamine B, and their mixture in 270, 180, and 480 s, respectively. In 2016, Sun and co-workers were the first to employed ZIF-8 derived carbon as a high-efficiency counter electrode for dye-sensitized solar cell [179]. A power conversion efficiency of 7.32% was achieved, which was comparable to that of platinum electrode (7.53%) measured under the same conditions. In 2017, Xie and co-workers developed CoNi@CNTs embedded carbon nanocages for the same application in dye-sensitized solar cells through pyrolysis of ZIF-67 [180]. A remarkable power conversion efficiency of 9.04% was achieved, as compared to the 7.88% achieved by platinum counter electrode. Lastly, non-porous Mg-MOF was used to prepare Mg nanoparticles imbedded carbon matrix and porous carbon/Mg hybrid for effective post-combustion carbon dioxide capture [181]. The as-synthesized compounds exhibited permanent porosity which selectively adsorb CO_2 over nitrogen at mild conditions. The authors suggested that the porosity depend more on the thermal stability of the framework during decomposition rather than the pristine structure topology of the template MOFs. Many researchers would come into agreement with this suggestion because like Cu-BTC, not all MOFs would produce nanostructures with the same porosity after heat treatment.

6. Conclusions and outlook

MOFs are a class of porous materials that exhibit high surface area, well defined pore size, and have a hybrid organic-inorganic nature. MOFs have demonstrated their potential applications in the fields ranging from gas storage and separation, energy storage, catalysis, drug delivery to chemical sensing and photonics. Recently, it has been demonstrated that MOFs can be used as sacrificial templates/precursors for the preparation of various inorganic nanostructures. The one-step pyrolysis of MOFs has been deemed as an effective route for fabrication of porous carbons, metal, metal oxides, and their multi-component hybrids. In this review, the successful potential applications of MOF-derived nanostructures in electrochemical energy storage, catalysis, sensing and other industries has been summarized. It is possible to tailor the structures and functionalities of these nanostructures for targeted applications by employing different

ligands, metallic centers and pyrolysis at various temperatures. Subsequently, these strategies have enabled the production of highly dispersed nanostructures with superior or at least comparable performance with structures obtained from other synthesis methods.

Based on the review, it can be concluded that ZIF-8 derived carbon materials generally have the highest surface area which is desirable for electrochemical energy storage. When tested for use in supercapacitors, Co-MOF (such as ZIF-67) derived nanostructures achieved the highest specific capacitance (~1400 F g^{-1}). Furthermore, the synergistic effects of bimetallic nanostructures resulting from metal doping of MOFs has appeared to be the most effective strategy to improve charge–discharge cycling stability of the porous materials. Remarkably, Co-MOF derived nanostructures could also be used as the positive electrode materials for LIBs due to their reversible high capacities. However, unless coated on a 3D substrate support such as the nickel foam, the stabilities of these Co-MOF derived nanostructures are inferior compared to MIL-125 derived Anatase TiO_2. Anatase TiO_2 derived from MIL-125 have had the smallest pore sizes and best stability under high current density, but they tend to achieve the lowest capacity when compared to other metal oxides. Therefore, more research is needed to synthesize MOF-derived nanostructures for further improved electrochemical performance with an optimum balance between high specific energy capacity and high stability.

Furthermore, ZIF family, especially ZIF-67 and ZIF-9, which are relatively easy to synthesize, are widely used as precursors to synthesize electrocatalyst for ORR, OER, and HER when compared to other MOF structures. Various improvement strategies have been applied to improve the performances of these electrocatalysts. The most practical and significant improvement strategy is heteroatom doping. That is effectively demonstrated when carbon materials doped with heteroatoms, such as N, P, or B, have resulted in more active sites present on the carbon materials. Recently, sulfur doping has also been proven to be able to increase cycling stability and promote the overall catalytic activity of MOF-derived carbon materials. With the structural and compositional advantages, MOF-derived electrocatalysts have showed some enhanced activities in comparison with the commercially available Pt/C catalyst. Besides, some of the MOFs, such as ZIF-67, ZIF-8, MIL-125 and Cu-BTC, have also been proven to be useful precursors for derivation of photocatalysts and catalysts for the production of fine chemicals. Some of these MOF-derived nanomaterials have also found applications in the field of wastewater treatment. Co-MOF is one of the widely-used MOF precursors due to the unique properties of the materials derived from it. The Co-MOF derived catalysts can be easily recycled (through magnetic separation) and has high product selectivity. Other less common MOF precursors, such as Mg-MOF, MIL-101, Ce-BTC, and Ni-BDC, had also been applied for the synthesis of nanomaterials for gas sensing and supercapacitors. Notably, CeO_2 derived from MOFs has received some research interests recently due to its anticorrosion property and high oxygen-storage capacity.

Currently, the main challenges in preparation and applications of MOF-derived materials lay in the needs to (1) improve the formulation and processing of MOF precursors and (2) better understand the formation mechanisms of the various nanostructures produced from the thermal decomposition of the MOFs. Besides, the structural stability of some MOF-derived nanostructures is low in comparison with the pristine nanostructures. A better control of pore sizes and volumes and more uniform exposure of active sites, especially those resulting from collapse of porous structures is also needed. In summary, the outlook for utilization of the MOF-derived nanostructures is positive. Efforts which had been devoted for the design and improvement of the performance of MOF-derived nanostructures, such as carbon capping, nitrogen doping, and bimetallic oxides functionalization, will continue to improve the application opportunity of these MOF-derived nanostructures in the field of electrochemical energy storage, heterogeneous catalysis and sensing.

Conflict of interest

The authors declare no conflict of interest.

Acknowledgements

The authors would like to thank for the financial support from Ningbo Municipal Government (Innovation Team 2012B82011, 3315 Plan, 2014A35001-1), and the EPSRC (EP/J000582/1, GR/R68078).

References

[1] H. Furukawa, K.E. Cordova, M. O'Keeffe, O.M. Yaghi, Science 341 (2013) 1230444.
[2] P. Silva, S.M.F. Vilela, J.P.C. Tome, F.A. Almeida Paz, Chem. Soc. Rev. 44 (2015) 6774–6803.
[3] J.-Y. Wu, T.-C. Chao, M.-S. Zhong, Cryst. Growth Des. 13 (2013) 2953–2964.
[4] Y. Zhang, X. Bo, A. Nsabimana, C. Han, M. Li, L. Guo, J. Mater. Chem. A 3 (2015) 732–738.
[5] N. Campagnol, E.R. Souza, D.E. De Vos, K. Binnemans, J. Fransaer, Chem. Commun. 50 (2014) 12545–12547.
[6] M.Y. Masoomi, A. Morsali, P.C. Junk, Cryst. Eng. Comm. 17 (2015) 686–692.
[7] N.A. Khan, S.H. Jhung, Coord. Chem. Rev. 285 (2015) 11–23.
[8] B. Seoane, S. Castellanos, A. Dikhtiarenko, F. Kapteijn, J. Gascon, Coord. Chem. Rev. 307 (Part 2) (2016) 147–187.
[9] B. Li, M. Chrzanowski, Y. Zhang, S. Ma, Coord. Chem. Rev. 307 (Part 2) (2016) 106–129.
[10] K.K. Gangu, S. Maddila, S.B. Mukkamala, S.B. Jonnalagadda, Inorganica Chim. Acta 446 (2016) 61–74.
[11] S.S.-Y. Chui, S.M.-F. Lo, J.P.H. Charmant, A.G. Orpen, I.D. Williams, Science 283 (1999) 1148–1150.
[12] H.D. Mai, K. Rafiq, H. Yoo, Chem. A Eur. J. 23 (2017) 5631–5651.
[13] J.A. Martens, J. Jammaer, S. Bajpe, A. Aerts, Y. Lorgouilloux, C.E.A. Kirschhock, Microporous Mesoporous Mater. 140 (2011) 2–8.
[14] N. Pal, A. Bhaumik, Adv. Colloid Interface Sci. 189–190 (2013) 21–41.
[15] W. Chaikittisilp, K. Ariga, Y. Yamauchi, J. Mater. Chem. A 1 (2013) 14–19.
[16] C. Liang, Z. Li, S. Dai, Angew. Chem. Int. Ed. 47 (2008) 3696–3717.
[17] W. Xia, A. Mahmood, R. Zou, Q. Xu, Energy Environ. Sci. 8 (2015) 1837–1866.

[18] X. Zhang, X. Cheng, Q. Zhang, J. Energy Chem. 25 (2016) 967–984.
[19] S. Goriparti, E. Miele, F. De Angelis, E. Di Fabrizio, R. Proietti Zaccaria, C. Capiglia, J. Power Sources 257 (2014) 421–443.
[20] Y. Liu, J. Xu, S. Liu, Microporous Mesoporous Mater. 236 (2016) 94–99.
[21] G.Z. Chen, Int. Mater. Rev. 62 (2017) 173–202.
[22] C. Alexander, C.K. Alexander, M. Sadiku, Fundamentals of Electric Circuits, McGraw-Hill Higher Education, 2006.
[23] X. Peng, L. Peng, C. Wu, Y. Xie, Chem. Soc. Rev. 43 (2014) 3303–3323.
[24] G. Wang, L. Zhang, J. Zhang, Chem. Soc. Rev. 41 (2012) 797–828.
[25] S. Zhong, C. Zhan, D. Cao, Carbon 85 (2015) 51–59.
[26] Y. Wang, B. Chen, Y. Zhang, L. Fu, Y. Zhu, L. Zhang, Y. Wu, Electrochim. Acta 213 (2016) 260–269.
[27] B. Guo, Y. Yang, Z. Hu, Y. An, Q. Zhang, X. Yang, X. Wang, H. Wu, Electrochim. Acta 223 (2017) 74–84.
[28] Y.-Z. Zhang, Y. Wang, Y.-L. Xie, T. Cheng, W.-Y. Lai, H. Pang, W. Huang, Nanoscale 6 (2014) 14354–14359.
[29] H. Hu, B. Guan, B. Xia, X.W. Lou, J. Am. Chem. Soc. 137 (2015) 5590–5595.
[30] Z. Jiang, W. Lu, Z. Li, K.H. Ho, X. Li, X. Jiao, D. Chen, J. Mater. Chem. A 2 (23) (2014) 8603–8606.
[31] H. Hu, Bu Y. Guan, Xiong W. Lou, Chem 1 (1) (2016) 102–113.
[32] B.Y. Guan, L. Yu, X. Wang, S. Song, X.W. Lou, Adv. Mater. 29 (6) (2017) 1605051.
[33] L. Shen, L. Yu, H.B. Wu, X.-Y. Yu, X. Zhang, X.W. Lou, Nat. Commun. 6 (2015) 6694.
[34] H. Chen, J. Jiang, Y. Zhao, L. Zhang, D. Guo, D. Xia, J. Mater. Chem. A 3 (1) (2015) 428–437.
[35] L. Shen, J. Wang, G. Xu, H. Li, H. Dou, X. Zhang, Adv. Energy Mater. 5 (3) (2015) 1400977.
[36] Y.C. Wang, W.B. Li, L. Zhao, B.Q. Xu, Phys. Chem. Chem. Phys. 18 (2016) 17941–17948.
[37] Y. Han, S. Zhang, N. Shen, D. Li, X. Li, Mater. Lett. 188 (2017) 1–4.
[38] M.-S. Wu, W.-H. Hsu, J. Power Sources 274 (2015) 1055–1062.
[39] G. Zeng, Y. Chen, L. Chen, P. Xiong, M. Wei, Electrochim. Acta 222 (2016) 773–780.
[40] S. Ullah, I.A. Khan, M. Choucair, A. Badshah, I. Khan, M.A. Nadeem, Electrochim. Acta 171 (2015) 142–149.
[41] L. Wang, Y. Han, X. Feng, J. Zhou, P. Qi, B. Wang, Coord. Chem. Rev. 307 (Part 2) (2016) 361–381.
[42] C. Ma, X. Shao, D. Cao, J. Mater. Chem. 22 (2012) 8911–8915.
[43] X. Wang, Q. Weng, X. Liu, X. Wang, D.-M. Tang, W. Tian, C. Zhang, W. Yi, D. Liu, Y. Bando, D. Golberg, Nano Lett. 14 (2014) 1164–1171.
[44] F. Zheng, Y. Yang, Q. Chen, Nat. Commun. 5 (2014) 5261.
[45] H. Wang, C. Zhang, Z. Liu, L. Wang, P. Han, H. Xu, K. Zhang, S. Dong, J. Yao, G. Cui, J. Mater. Chem. 21 (2011) 5430–5434.
[46] S.J. Yang, S. Nam, T. Kim, J.H. Im, H. Jung, J.H. Kang, S. Wi, B. Park, C.R. Park, J. Am. Chem. Soc. 135 (2013) 7394–7397.
[47] X. Sun, C. Zhou, M. Xie, H. Sun, T. Hu, F. Lu, S.M. Scott, S.M. George, J. Lian, J. Mater. Chem. A 2 (2014) 7319–7326.
[48] Y. Song, Y. Chen, J. Wu, Y. Fu, R. Zhou, S. Chen, L. Wang, J. Alloys Compd. 694 (2017) 1246–1253.
[49] H. Yue, Z. Shi, Q. Wang, Z. Cao, H. Dong, Y. Qiao, Y. Yin, S. Yang, ACS Appl. Mater. Interfaces 6 (2014) 17067–17074.
[50] S. Gao, R. Fan, B. Li, L. Qiang, Y. Yang, Electrochim. Acta 215 (2016) 171–178.
[51] Y. Zou, Z. Qi, Z. Ma, W. Jiang, R. Hu, J. Duan, J. Electroanal. Chem. 788 (2017) 184–191.
[52] F. Zou, X. Hu, Z. Li, L. Qie, C. Hu, R. Zeng, Y. Jiang, Y. Huang, Adv. Mater. 26 (2014) 6622–6628.
[53] D. Cai, H. Zhan, T. Wang, Mater. Lett. 197 (2017) 241–244.
[54] M. Du, D. He, Y. Lou, J. Chen, J. Energy Chem. (2017) 1–8.
[55] P. Su, S. Liao, F. Rong, F. Wang, J. Chen, C. Li, Q. Yang, J. Mater. Chem. A 2 (2014) 17408–17414.
[56] G. Fang, J. Zhou, C. Liang, A. Pan, C. Zhang, Y. Tang, X. Tan, J. Liu, S. Liang, Nano Energy 26 (2016) 57–65.
[57] H. Hu, J. Zhang, B. Guan, X.W. Lou, Angew. Chem. Int. Ed. 55 (33) (2016) 9514–9518.
[58] L. Yu, J.F. Yang, X.W. Lou, Angew. Chem. Int. Ed. 55 (43) (2016) 13422–13426.
[59] H. Pang, W. Sun, L.-P. Lv, F. Jin, Y. Wang, J. Mater. Chem. A 4 (48) (2016) 19179–19188.
[60] L. Xu, Y. Hu, H. Zhang, H. Jiang, C. Li, ACS Sustain. Chem. Eng. 4 (8) (2016) 4251–4255.
[61] F. Jin, Y. Wang, J. Mater. Chem. A 3 (28) (2015) 14741–14749.
[62] H. Xue, D.Y.W. Yu, J. Qing, X. Yang, J. Xu, Z. Li, M. Sun, W. Kang, Y. Tang, C.-S. Lee, J. Mater. Chem. A 3 (15) (2015) 7945–7949.
[63] G. Li, H. Yang, F. Li, J. Du, W. Shi, P. Cheng, J. Mater. Chem. A 4 (24) (2016) 9593–9599.
[64] M. Wang, H. Yang, X. Zhou, W. Shi, Z. Zhou, P. Cheng, Chem. Commun. 52 (4) (2016) 717–720.
[65] D. Ji, H. Zhou, Y. Tong, J. Wang, M. Zhu, T. Chen, A. Yuan, Chem. Eng. J. 313 (2017) 1623–1632.
[66] R. Wu, X. Qian, F. Yu, H. Liu, K. Zhou, J. Wei, Y. Huang, J. Mater. Chem. A 1 (2013) 11126–11129.
[67] Z. Xiu, M.H. Alfaruqi, J. Gim, J. Song, S. Kim, P.T. Duong, J.P. Baboo, V. Mathew, J. Kim, J. Alloys Compd. 674 (2016) 174–178.
[68] Z. Wang, X. Li, H. Xu, Y. Yang, Y. Cui, H. Pan, Z. Wang, B. Chen, G. Qian, J. Mater. Chem. A 2 (2014) 12571–12575.
[69] J.R. Dahn, T. Zheng, Y. Liu, J.S. Xue, Science 270 (1995) 590–593.
[70] Z. Li, L. Yin, ACS Appl. Mater. Interfaces 7 (2015) 4029–4038.
[71] X. Li, Q. Sun, J. Liu, B. Xiao, R. Li, X. Sun, J. Power Sources 302 (2016) 174–179.
[72] M.J. Song, I.T. Kim, Y.B. Kim, J. Kim, M.W. Shin, Electrochim. Acta 230 (2017) 73–80.
[73] W. Yin, Y. Shen, F. Zou, X. Hu, B. Chi, Y. Huang, ACS Appl. Mater. Interfaces 7 (2015) 4947–4954.
[74] T. Liu, M. Jia, Y. Zhang, J. Han, Y. Li, S. Bao, D. Liu, J. Jiang, M. Xu, J. Power Sources 341 (2017) 53–59.
[75] J. Hagen, Future Development of Catalysis, Industrial Catalysis, Wiley-VCH Verlag GmbH & Co. KGaA, 2015, pp. 463–472.
[76] S. Bhaduri, D. Mukesh, Chemical Industry and Homogeneous Catalysis, Homogeneous Catalysis, John Wiley & Sons, Inc, 2014, pp. 1–21.
[77] S.H.Y.S. Abdullah, N.H.M. Hanapi, A. Azid, R. Umar, H. Juahir, H. Khatoon, A. Endut, Renew. Sustain. Energy Rev. 70 (2017) 1040–1051.
[78] J. Liu, L. Chen, H. Cui, J. Zhang, L. Zhang, C.-Y. Su, Chem. Soc. Rev. 43 (2014) 6011–6061.
[79] Y.-B. Huang, J. Liang, X.-S. Wang, R. Cao, Chem. Soc. Rev. 46 (1) (2017) 126–157.
[80] M.A. Nasalevich, M. van der Veen, F. Kapteijn, J. Gascon, Cryst. Eng. Comm. 16 (2014) 4919–4926.
[81] Y. Yusran, D. Xu, Q. Fang, D. Zhang, S. Qiu, Microporous Mesoporous Mater. 241 (2017) 346–354.
[82] Y. Kang, P. Yang, N.M. Markovic, V.R. Stamenkovic, Nano Today 11 (5) (2016) 587–600.
[83] C. Song, J. Zhang, Electrocatalytic oxygen reduction reaction, in: J. Zhang (Ed.), PEM Fuel Cell Electrocatalysts and Catalyst Layers: Fundamentals and Applications, Springer London, London, 2008, pp. 89–134.
[84] L. Trotochaud, S.W. Boettcher, Scr. Mater. 74 (2014) 25–32.
[85] M.G. Walter, E.L. Warren, J.R. McKone, S.W. Boettcher, Q. Mi, E.A. Santori, N.S. Lewis, Chem. Rev. 110 (11) (2010) 6446–6473.
[86] F. Afsahi, H. Vinh-Thang, S. Mikhailenko, S. Kaliaguine, J. Power Sources 239 (2013) 415–423.
[87] D. Zhao, J.-L. Shui, C. Chen, X. Chen, B.M. Reprogle, D. Wang, D.-J. Liu, Chem. Sci. 3 (2012) 3200–3205.
[88] S. Ma, G.A. Goenaga, A.V. Call, D.-J. Liu, Chem. A Eur. J. 17 (2011) 2063–2067.
[89] W. Chaikittisilp, N.L. Torad, C. Li, M. Imura, N. Suzuki, S. Ishihara, K. Ariga, Y. Yamauchi, Chem. A Eur. J. 20 (15) (2014) 4217–4221.
[90] W. Xia, J. Zhu, W. Guo, L. An, D. Xia, R. Zou, J. Mater. Chem. A 2 (2014) 11606–11613.
[91] W. Xia, R. Zou, L. An, D. Xia, S. Guo, Energy Environ. Sci. 8 (2015) 568–576.

[92] B. You, N. Jiang, M. Sheng, W.S. Drisdell, J. Yano, Y. Sun, ACS Catal. 5 (2015) 7068–7076.
[93] L. Shang, H. Yu, X. Huang, T. Bian, R. Shi, Y. Zhao, G.I.N. Waterhouse, L.-Z. Wu, C.-H. Tung, T. Zhang, Adv. Mater. 28 (2016) 1668–1674.
[94] P. He, X.-Y. Yu, X.W. Lou, Angew. Chem. Int. Ed. 56 (14) (2017) 3897–3900.
[95] D. Li, H. Baydoun, C.N. Verani, S.L. Brock, J. Am. Chem. Soc. 138 (12) (2016) 4006–4009.
[96] L. Jiao, Y.-X. Zhou, H.-L. Jiang, Chem. Sci. 7 (3) (2016) 1690–1695.
[97] L.-A. Stern, L. Feng, F. Song, X. Hu, Energy Environ. Sci. 8 (8) (2015) 2347–2351.
[98] L. Han, X.-Y. Yu, X.W. Lou, Adv. Mater. 28 (23) (2016) 4601–4605.
[99] X. Li, Y. Fang, X. Lin, M. Tian, X. An, Y. Fu, R. Li, J. Jin, J. Ma, J. Mater. Chem. A 3 (2015) 17392–17402.
[100] H.-S. Lu, H. Zhang, R. Liu, X. Zhang, H. Zhao, G. Wang, Appl. Surf. Sci. 392 (2017) 402–409.
[101] Y. Dong, M. Yu, Z. Wang, T. Zhou, Y. Liu, X. Wang, Z. Zhao, J. Qiu, Energy Storage Mater. 7 (2017) 181–188.
[102] Y. Hou, Z. Wen, S. Cui, S. Ci, S. Mao, J. Chen, Adv. Funct. Mater. 25 (2015) 872–882.
[103] B. Chen, G. Ma, Y. Zhu, J. Wang, W. Xiong, Y. Xia, J. Power Sources 334 (2016) 112–119.
[104] F. Ming, H. Liang, H. Shi, X. Xu, G. Mei, Z. Wang, J. Mater. Chem. A 4 (39) (2016) 15148–15155.
[105] X.-Y. Yu, Y. Feng, B. Guan, X.W. Lou, U. Paik, Energy Environ. Sci. 9 (4) (2016) 1246–1250.
[106] X. Li, Y. Fang, F. Li, M. Tian, X. Long, J. Jin, J. Ma, J. Mater. Chem. A 4 (40) (2016) 15501–15510.
[107] S. Wu, X. Shen, G. Zhu, H. Zhou, Z. Ji, L. Ma, K. Xu, J. Yang, A. Yuan, Carbon 116 (2017) 68–76.
[108] X. Mao, J. Kwon, E.K. Koh, D.Y. Hwang, J. Lee, ACS Appl. Mater. Interfaces 7 (2015) 15522–15530.
[109] H. Zhang, Z. Ma, J. Duan, H. Liu, G. Liu, T. Wang, K. Chang, M. Li, L. Shi, X. Meng, K. Wu, J. Ye, ACS Nano 10 (2016) 684–694.
[110] W. Zhou, J. Lu, K. Zhou, L. Yang, Y. Ke, Z. Tang, S. Chen, Nano Energy 28 (2016) 143–150.
[111] J.-B. Raoof, S.R. Hosseini, R. Ojani, S. Mandegarzad, Energy 90 (Part 1) (2015) 1075–1081.
[112] S. Mandegarzad, J.B. Raoof, S.R. Hosseini, R. Ojani, Electrochim. Acta 190 (2016) 729–736.
[113] H. Ren, P. Koshy, W.-F. Chen, S. Qi, C.C. Sorrell, J. Hazard. Mater. 325 (2017) 340–366.
[114] N.M. Gupta, Renew. Sustain. Energy Rev. 71 (2017) 585–601.
[115] Y. Izumi, Coord. Chem. Rev. 257 (2013) 171–186.
[116] K.M. Lee, C.W. Lai, K.S. Ngai, J.C. Juan, Water Res. 88 (2016) 428–448.
[117] N.P. Radhika, R. Selvin, R. Kakkar, A. Umar, Arabian J. Chem. (2016), http://dx.doi.org/10.1016/j.arabjc.2016.07.007.
[118] M. Bellardita, H.A.E. Nazer, V. Loddo, F. Parrino, A.M. Venezia, L. Palmisano, Catal. Today 284 (2017) 92–99.
[119] X. Wang, M. Kimling, R. Caruso, Preparation of nanoporous semiconductor-based materials for photocatalytic applications, in: Nanoporous Materials, CRC Press, 2013, pp. 201–236.
[120] L. Shen, R. Liang, L. Wu, Chin. J. Catal. 36 (2015) 2071–2088.
[121] Y. Du, R.Z. Chen, J.F. Yao, H.T. Wang, J. Alloys Compd. 551 (2013) 125–130.
[122] L. Pan, T. Muhammad, L. Ma, Z.-F. Huang, S. Wang, L. Wang, J.-J. Zou, X. Zhang, Appl. Catal. B Environ. 189 (2016) 181–191.
[123] Y. Feng, H. Lu, X. Gu, J. Qiu, M. Jia, C. Huang, J. Yao, J. Phys. Chem. Solids 102 (2017) 110–114.
[124] G. Zhu, X. Li, H. Wang, L. Zhang, Catal. Commun. 88 (2017) 5–8.
[125] Y. Zhang, J. Huang, Y. Ding, Appl. Catal. B Environ. 198 (2016) 447–456.
[126] J.-Y. Xu, X.-P. Zhai, L.-F. Gao, P. Chen, M. Zhao, H.-B. Yang, D.-F. Cao, Q. Wang, H.-L. Zhang, RSC Adv. 6 (2016) 2011–2018.
[127] C.Y. Lee, O.K. Farha, B.J. Hong, A.A. Sarjeant, S.T. Nguyen, J.T. Hupp, J. Am. Chem. Soc. 133 (2011) 15858–15861.
[128] C. Wang, K.E. deKrafft, W. Lin, J. Am. Chem. Soc. 134 (2012) 7211–7214.
[129] D.P. Kumar, J. Choi, S. Hong, D.A. Reddy, S. Lee, T.K. Kim, ACS Sustain. Chem. Eng. 4 (2016) 7158–7166.
[130] J. Li, X. Xu, X. Liu, W. Qin, M. Wang, L. Pan, J. Alloys Compd. 690 (2017) 640–646.
[131] A. Dhakshinamoorthy, M. Opanasenko, J. Cejka, H. Garcia, Catal. Sci. Technol. 3 (2013) 2509–2540.
[132] B.R. Pimentel, A. Parulkar, E.-k. Zhou, N.A. Brunelli, R.P. Lively, ChemSusChem 7 (2014) 3202–3240.
[133] X. Li, C. Zeng, J. Jiang, L. Ai, J. Mater. Chem. A 4 (2016) 7476–7482.
[134] X. Wang, Y. Li, J. Mol. Catal. A Chem. 420 (2016) 56–65.
[135] K.-Y.A. Lin, H.-A. Chang, R.-C. Chen, Chemosphere 130 (2015) 66–72.
[136] K.-Y. Andrew Lin, B.-C. Chen, Dalton Trans. 45 (8) (2016) 3541–3551.
[137] W. Zhong, H. Liu, C. Bai, S. Liao, Y. Li, ACS Catal. 5 (2015) 1850–1856.
[138] C. Bai, A. Li, X. Yao, H. Liu, Y. Li, Green Chem. 18 (2016) 1061–1069.
[139] X. Wang, Y. Li, J. Mater. Chem. A 4 (2016) 5247–5257.
[140] G. Yu, J. Sun, F. Muhammad, P. Wang, G. Zhu, RSC Adv. 4 (2014) 38804–38811.
[141] E. Rose, B. Andrioletti, S. Zrig, M. Quelquejeu-Etheve, Chem. Soc. Rev. 34 (2005) 573–583.
[142] J. Sun, G. Yu, L. Liu, Z. Li, Q. Kan, Q. Huo, J. Guan, Catal. Sci. Technol. 4 (2014) 1246–1252.
[143] D. Zhou, B. Tang, X.H. Lu, X.L. Wei, K. Li, Q.H. Xia, Catal. Commun. 45 (2014) 124–128.
[144] X. Li, J. Zhang, W. Li, J. Ind. Eng. Chem. 44 (2016) 146–154.
[145] S. Chao, F. Zou, F. Wan, X. Dong, Y. Wang, Y. Wang, Q. Guan, G. Wang, W. Li, Sci. Rep. 7 (2017) 39789.
[146] R. Zhang, L. Hu, S. Bao, R. Li, L. Gao, R. Li, Q. Chen, J. Mater. Chem. A 4 (2016) 8412–8420.
[147] H. Niu, S. Liu, Y. Cai, F. Wu, X. Zhao, Microporous Mesoporous Mater. 219 (2016) 48–53.
[148] S. Gao, X. Jia, J. Yang, X. Wei, J. Mater. Chem. 22 (2012) 21733–21739.
[149] T. Wu, L. Zhang, J. Gao, Y. Liu, C. Gao, J. Yan, J. Mater. Chem. A 1 (2013) 7384–7390.
[150] M.J. Kim, B.R. Kim, C.Y. Lee, J. Kim, Tetrahedron Lett. 57 (2016) 4070–4073.
[151] Y.-H. Qin, L. Huang, D.-L. Zhang, L.-G. Sun, Inorg. Chem. Commun. 66 (2016) 64–68.
[152] Y. Wang, S. Sang, W. Zhu, L. Gao, G. Xiao, Chem. Eng. J. 299 (2016) 104–111.
[153] X. Yao, C. Bai, J. Chen, Y. Li, RSC Adv. 6 (2016) 26921–26928.
[154] S. Cheng, N. Shang, C. Feng, S. Gao, C. Wang, Z. Wang, Catal. Commun. 89 (2017) 91–95.
[155] Y. Zhou, J. Long, Y. Li, Chin. J. Catal. 37 (2016) 955–962.
[156] S. Li, N. Wang, Y. Yue, G. Wang, Z. Zu, Y. Zhang, Chem. Sci. 6 (2015) 2495–2500.
[157] V.P. Santos, T.A. Wezendonk, J.J.D. Jaén, A.I. Dugulan, M.A. Nasalevich, H.-U. Islam, A. Chojecki, S. Sartipi, X. Sun, A.A. Hakeem, A.C.J. Koeken, M. Ruitenbeek, T. Davidian, G.R. Meima, G. Sankar, F. Kapteijn, M. Makkee, J. Gascon, Nat. Commun. 6 (2015) 6451.
[158] P. Kumar, A. Deep, K.-H. Kim, TrAC Trends Anal. Chem. 73 (2015) 39–53.
[159] G. Korotcenkov, B.K. Cho, Sens. Actuators B Chem. 244 (2017) 182–210.
[160] W. Li, X. Wu, N. Han, J. Chen, X. Qian, Y. Deng, W. Tang, Y. Chen, Sens. Actuators B Chem. 225 (2016) 158–166.
[161] W. Li, X. Wu, N. Han, J. Chen, W. Tang, Y. Chen, Powder Technol. 304 (2016) 241–247.
[162] J.M. Xu, J.P. Cheng, J. Alloys Compd. 686 (2016) 753–768.
[163] F. Qu, H. Jiang, M. Yang, Mater. Lett. 190 (2017) 75–78.
[164] H. Tan, C. Ma, L. Gao, Q. Li, Y. Song, F. Xu, T. Wang, L. Wang, Chem. – A Eur. J. 20 (2014) 16377–16383.

[165] H. Tan, G. Tang, Z. Wang, Q. Li, J. Gao, S. Wu, Anal. Chim. Acta 940 (2016) 136–142.
[166] S. De Gisi, G. Lofrano, M. Grassi, M. Notarnicola, Sustain. Mater. Technol. 9 (2016) 10–40.
[167] B.N. Bhadra, I. Ahmed, S. Kim, S.H. Jhung, Chem. Eng. J. 314 (2017) 50–58.
[168] I. Ahmed, B.N. Bhadra, H.J. Lee, S.H. Jhung, Catal. Today (2017), http://dx.doi.org/10.1016/j.cattod.2017.02.011.
[169] S. Li, X. Zhang, Y. Huang, J. Hazard. Mater. 321 (2017) 711–719.
[170] N. Bakhtiari, S. Azizian, S.M. Alshehri, N.L. Torad, V. Malgras, Y. Yamauchi, Microporous Mesoporous Mater. 217 (2015) 173–177.
[171] X. Liu, C. Wang, Z. Wang, Q. Wu, Z. Wang, Microchim. Acta 182 (2015) 1903–1910.
[172] C.B. Vidal, M. Seredych, E. Rodríguez-Castellón, R.F. Nascimento, T.J. Bandosz, J. Colloid Interface Sci. 449 (2015) 180–191.
[173] V. Calisto, C.I.A. Ferreira, J.A.B.P. Oliveira, M. Otero, V.I. Esteves, J. Environ. Manag. 152 (2015) 83–90.
[174] H. Chen, B. Gao, H. Li, J. Hazard. Mater. 282 (2015) 201–207.
[175] M.J. Ahmed, S.K. Theydan, J. Taiwan Inst. Chem. Eng. 45 (2014) 219–226.
[176] F. Yu, S. Sun, S. Han, J. Zheng, J. Ma, Chem. Eng. J. 285 (2016) 588–595.
[177] X. Cui, W. Zuo, M. Tian, Z. Dong, J. Ma, J. Mol. Catal. A Chem. 423 (2016) 386–392.
[178] Z. Hasan, D.-W. Cho, G.J. Islam, H. Song, J. Alloys Compd. 689 (2016) 625–631.
[179] X. Sun, Y. Li, J. Dou, D. Shen, M. Wei, J. Power Sources 322 (2016) 93–98.
[180] Z. Xie, X. Cui, W. Xu, Y. Wang, Electrochim. Acta 229 (2017) 361–370.
[181] Y. He, J. Shang, Q. Zhao, Q. Gu, K. Xie, G. Li, R. Singh, P. Xiao, P.A. Webley, Polyhedron 120 (2016) 30–35.